Searches for pulsar-like candidates from unidentified objects in the Third Catalog of Hard *Fermi*-LAT Sources with machine learning techniques

C. Y. Hui [1],[*] Jongsu Lee,[2] K. L. Li,[1,3,4] Sangin Kim,[2] Kwangmin Oh,[2] Shengda Luo,[5] Alex P. Leung,[5] A. K. H. Kong [4], J. Takata[6] and K. S. Cheng[7]

[1]*Department of Astronomy and Space Science, Chungnam National University, Daejeon 34134, Korea*
[2]*Department of Space Science and Geology, Chungnam National University, Daejeon 34134, Korea*
[3]*Department of Physics, UNIST, Ulsan 44919, Korea*
[4]*Institute of Astronomy, National Tsing Hua University, Hsinchu 30013, Taiwan*
[5]*Faculty of Information Technology, Macau University of Science and Technology, Avenida Wai Long, Taipa, Macau*
[6]*School of Physics, Huazhong University of Science and Technology,Wuhan, 430074 PR China*
[7]*Department of Physics, University of Hong Kong, Pokfulam Road, Hong Kong*

ABSTRACT

We report the results of searching pulsar-like candidates from the unidentified objects in the Third Catalog of Hard *Fermi*-LAT Sources (3FHL). Using a machine-learning-based classification scheme with a nominal accuracy of ~ 98 per cent, we have selected 27 pulsar-like objects from 200 unidentified 3FHL sources for an identification campaign. Using archival data, X-ray sources are found within the γ-ray error ellipses of 10 3FHL pulsar-like candidates. Within the error circles of the much better constrained X-ray positions, we have also searched for the optical/infrared counterparts and examined their spectral energy distributions. Among our shortlisted candidates, the most secure identification is the association of 3FHL J1823.3–1339 and its X-ray counterpart with the globular cluster Mercer 5. The γ-rays from the source can be contributed by a population of millisecond pulsars residing in the cluster. This makes Mercer 5 as one of the slowly growing hard γ-ray population of globular clusters with emission >10 GeV. Very recently, another candidate picked by our classification scheme, 3FHL J1405.1–6118, has been identified as a new γ-ray binary with an orbital period of 13.7 d. Our X-ray analysis with a short *Chandra* observation has found a possible periodic signal candidate of ~ 1.4 h and a putative extended X-ray tail of ~ 20 arcsec long. Spectral energy distribution of its optical/infrared counterpart conforms with a blackbody of $T_{bb} \sim 40\,000$ K and $R_{bb} \sim 12\,\mathrm{R}_\odot$ at a distance of 7.7 kpc. This is consistent with its identification as an early O star as found by infrared spectroscopy.

Key words: pulsars: general – gamma-rays: stars – X-rays: binaries – X-rays: stars.

1 INTRODUCTION

Fermi Gamma-ray Space Telescope has brought us into a new era of high-energy astronomy by significantly expanding the population of γ-ray sources. In particular for pulsars, thanks to the much improved sensitivity of the Large Area Telescope (LAT) on-board *Fermi*, our understandings of their high-energy properties have been advanced considerably in the last decade (see Hui 2018 for a recent review). Currently, there are 234 γ-ray pulsars have been detected, which is >30 times of their population before the launch of *Fermi*. Not only enlarging the population, *Fermi* LAT also has uncovered previously unknown classes of γ-ray pulsars (Abdo et al. 2013) such as millisecond pulsars (MSPs). Furthermore, other γ-ray phenomena

related to pulsars have also been found. For example, γ-ray emission was discovered from a number of globular clusters (Abdo et al. 2009; Kong, Hui & Cheng 2010; Tam et al. 2011), which can be originated from the collective contribution of the magnetospheric radiation from MSPs in the cluster (Abdo et al. 2010) and/or from the inverse Compton scattering between the relativistic pulsar wind outflow and the local soft photon field (Cheng et al. 2010; Hui et al. 2011). Also, flares in X-ray, GeV, and TeV regimes from the γ-ray binaries, which contain a pulsar and a OB companion, were detected before/after the periastron passage (e.g. Tam et al. 2018). These flares are suggested to be resulted from the intrabinary shocks (Takata et al. 2017).

In the previous *Fermi* LAT point source catalogues obtained from the full band all-sky survey (>100 MeV), there are approximately one-third of the sources have their nature unidentified (e.g. 2FGL: Nolan et al. 2012; 3FGL: Acero et al. 2015). The locations of these

[*] E-mail: huichungyue@gmail.com

unidentified *Fermi* objects provide us with a 'treasure map' for searching interesting objects with multiwavelength observations. By imposing a suitable set of classification criteria, one can select some promising candidates from these unidentified sources for searching the counterparts within their γ-ray positional error ellipses. For example, by choosing the unidentified objects that have low γ-ray flux variability for discriminating them from the active galactic nuclei (AGN)-like sources (i.e. small variability indices) and with curved spectral shape similar to the pulsars (i.e. large curvature significances), one can obtain a list of pulsar candidates for follow-up identifications (e.g. Kong et al. 2012; Hui et al. 2015; Saz Parkinson et al. 2016). A significant fraction of MSPs were discovered by this method (Clark 2017).

Apart from the full band γ-ray source catalogues, lists of sources in the hard γ-ray bands have also been compiled. In the Third Catalog of Hard *Fermi* LAT Sources (3FHL) (Ajello et al. 2017), it contains 1556 objects detected in the energy range of 10 GeV to 2 TeV. 136 of them have their nature identified and 1220 'associated' sources have been classified primarily by the positional coincidence with sources of known nature. Among these 1356 sources, 59 sources are labelled as pulsars and the rest includes mostly AGNs. The remaining 200 sources do not have any association/identification in the 3FHL catalogue.

A recent systematic investigation has been carried out for pinpointing the nature of these unidentified 3FHL objects (Kaur et al. 2019). They have selected 110 sources from 200 unidentified 3FHL sources that have their fields covered by archival *Swift*-X-Ray Telescope (XRT) data for their analysis. Among them, 52 sources have a single X-ray source detected in their 95 per cent γ-ray error ellipses and have been selected for further analysis. By cross-matching the X-ray positions with catalogues of different wavelengths, Kaur et al. (2019) have classified 36 of these sources as AGN candidates.

While their work is successful in identifying a number of AGN candidates, their approach is not very efficient as they have to analyse a large number of sources without any pre-screening. A lot of effort has been spent on analysing the data of the sources that are unlikely to be their target-of-interest (i.e. AGN). A more efficient approach is to select the promising candidates first with machine learning algorithms and then look into the archival data and/or carry follow-up observations afterward. This is the approach we adopted in our investigation.

In this work, we present a systematic search for pulsar-like candidates from the unassociated/unidentified 3FHL objects with machine learning techniques and performed a follow-up multiwavelength identification campaign. While the population of pulsars with energies >100 MeV has been significantly expanded, the population in the very high energy regime (VHE >100 GeV) remains to be rather small. So far only three pulsars have their pulsed emission detected at energies >50 GeV (cf. Hui 2018 for a review). Besides their magnetospheric radiation, interaction of the pulsar emission and/or wind particles with their surroundings can also produce VHE photons such as those in γ-ray binaries and globular clusters. The hard γ-ray pulsar-like candidates investigated in this work have the potential for enlarging VHE pulsar population and the related phenomena.

2 PSR-LIKE CANDIDATE SELECTION WITH MACHINE LEARNING TECHNIQUES

Using the 3FHL sources with identified/associated nature for training and testing a classifier, we can perform a binary classification of 3FHL sources between pulsars (PSR) and non-pulsars (NON_PSR) by employing machine learning techniques.

Among 65 features in the catalogue, 16 features were removed in the pre-processing stage. 11 features are manually removed as we believe they are not useful in determining the source nature, such as their 3FHL names and alternative names. We have also set a threshold of removing any feature with more than 10 per cent of null values, and five more features are therefore automatically removed.

We use 1356 identified/associated sources as our sample for the feature selection and building prediction models. Among them, 1231 γ-ray sources are identified/associated with extragalactic objects, which include starburst galaxy, BL Lac, flat-spectrum radio quasar type of blazar, non-blazar active galaxy, narrow-line Seyfert 1, radio galaxy, and blazar candidate of uncertain type. On the other hand, there are 125 γ-ray sources reside in our Galaxy. These Galactic 3FHL sources include pulsars, pulsar wind nebula, supernova remnant, high-mass binary, binary, globular clusters, and star formation regions. Since we are interested in looking for the pulsar-like candidates, we perform a one-against-all classification. Instead of using the original labels in the catalogue for identifying their nature, we add a column to divide them into two classes. For all the sources identified as (or associated with) pulsars, we put them in the class of 'PSR'. Otherwise, we label them as 'NON_PSR'.

In the previous work of selecting pulsar candidates from the unidentified *Fermi* objects, γ-ray flux variability is an important feature for us to distinguish the pulsar-like sources from the AGN-like sources (e.g. Hui et al. 2015). However, there is no feature for indicating variability in 3FHL catalogue. Instead of relying on our current knowledge for differentiating the γ-ray properties between pulsars and the other γ-ray sources, we employ an automatic feature selection algorithm (Leung et al. 2017; Luo et al. 2020) for picking the features that can help discriminate a source is PSR-like or not. We achieve this by adopting a scheme of recursive feature elimination (RFE). RFE is a backward selection method with unimportant features are sequentially eliminated during a recursive process (Leung et al. 2017). With this machine-learning-based technique, attributes and patterns of the data that are overlooked by human investigators can be highlighted.

After the pre-processing stage, an optimal set of features can be automatically selected by using RFE. For each iteration in the stage of RFE, we evaluate the performance of a random forest classifier by computing the root-mean-squared error (RMSE). The classification performance is evaluated by plotting the RMSE with the corresponding number of features. The performance profile produced by the RFE for the 3FHL catalogue is shown in Fig. 1. While the minimum of the profile is attained by using 30 out of all 49 features, it appears to be rather flat for the number of features $\gtrsim 15$. The minimum corrsponds to 30 features (i.e. solid blue symbol in Fig. 1) can be a result of local fluctuations.

In view of this, we chose to suffice a little bit of performance by accepting an upper margin of error of 5 per cent in the RMSE value to trade for a simpler model with better interpretability. A simpler model is often easier to understand and more robust (cf. Luo et al. 2020).

With this imposed scheme, a minimal set of 17 features is selected. The selected features are summarized in Table 1 that are ranked by their importance scores.

In Fig. 2, we show the two-dimensional projections of the feature space for the highly ranked features: Flux_Density_Error, Powerlaw_Index, and Pivot_Energy. The known PSR and NON_PSR sources in 3FHL catalogue are plotted as red dots and blue dots,
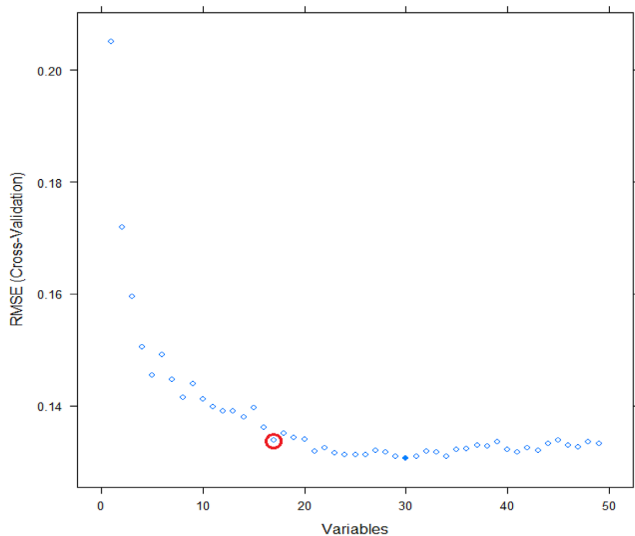
Figure 1. The performance profile of PSR/NON_PSR classification in the 3FHL catalogue. The optimal performance is achieved by using 30 features (solid symbol). Allowing a tolerance of 1.05 as the margin of error in the RMSE value, a minimal set of 17 features is selected for building the model that is highlighted by the circle.

Table 1. The rank of the features selected by RFE (Leung et al. 2017) for the 3FHL catalogue. Refer to Ajello et al. (2017) for the physical meanings of these features.

Features	Importance scores
Flux_Density_Error	15.76
Spectral_Index	15.08
Powerlaw_Index	14.76
Pivot_Energy	14.46
Flux_20_50_GeV_Neg_Err	8.85
Powerlaw_Index_Error	7.31
Flux_20_50_GeV	7.10
Flux_Density	7.08
BII	6.75
Conf_95_SemiMinor	6.74
Conf_95_SemiMajor	6.42
Flux_150_500_GeV_Pos_Err	6.35
Flux_10_20_GeV_Pos_Err	6.26
Curve_Significance	6.04
Flux_0p5_2_TeV	5.93
HEP_Prob	5.93
HEP_Energy	5.86

respectively. These chosen features suggest that the hardness of γ-rays is a key factor for differentiating PSR and NON_PSR sources. This can be readily shown by the distributions of the Powerlaw_Index/Spectral_Index (Fig. 2). The harder a source is, the smaller these features will be. On the other hand, Pivot_Energy is defined as the energy at which the error on differential photon flux is minimal (Ajello et al. 2017). A softer γ-ray source has a smaller Pivot_Energy, and therefore it anticorrelates with the Powerlaw_Index/Spectral_Index. For the feature Flux_Density_Error, it is the error on differential photon flux at Pivot_Energy (Ajello et al. 2017). For the hard sources, which have larger Pivot_Energy, their differential fluxes at Pivot_Energy tend to be smaller. Since Flux_Density_Error generally scales with the differential flux

(see Luo et al. 2020), this feature naturally anticorrelates with Pivot_Energy.

One surprising result is that the feature Curve_Significance, which many previous studies have relied on selecting pulsar candidates (Kong et al. 2012; Hui et al. 2015; Saz Parkinson et al. 2016), does not appear to be a highly ranked defining characteristic for pulsars in 3FHL catalogue. It has been found that the γ-ray spectra of most of the pulsars are characterized by a power law with an exponential cut-off at energies $\lesssim 5$ GeV (Abdo et al. 2013; Hui et al. 2017). As all the pulsars included the in 3FHL catalogue are detected in the energy range of 10 GeV to 2 TeV, which beyond the typical range of the spectral cut-off of most pulsars, their less curved spectra can be a selection effect. This may explain why Curve_Significance is not among the top-ranked features for discriminating pulsars from the others in hard γ-ray band.

Using the features in Table 1 to build the prediction model, we compare the performances of different classifiers. Seven prediction models are built with the following machine learning methods: random forest (RF), generalized additive models (GAM), logistic regression (LR), boosted logistic regression (Boost LR), support vector machines (SVM), decision trees (DT), and logistic trees (LT). For each of these tested classifiers, the data of labelled sources are randomly divided into training/test sets with a ratio of 70/30 per cent.

During the training stage, some parameters of various classifiers are tuned for optimizing their performances with the training data set as the input. Such parameters are automatically optimized by using a 10-fold cross-validation empirically. For quantifying the performance of each model, we compute the overall accuracy that is defined as the ratio of the correct classification in the test set. A comparison of the overall accuracies of different classifiers is summarized in Table 2. Among all the tested classifiers, an optimal overall accuracy of 98.03 per cent is achieved with RF. Using a scheme of nested cross-validation (Luo et al. 2020), we found that the standard deviations of all the quote accuracies in Table 2 are $\lesssim 1$ per cent.

To further characterize the model performance with RF, we computed the receiver operating characteristic (ROC) curves for the PSR/NON_PSR classification task with both training set and test set. ROC curve is a plot of sensitivity (i.e. probability of detection) against specificity (i.e. one probability of false alarm). A good model should minimize the false alarm and avoid missing any detection, and hence its ROC curve would be pushed toward the top left-hand corner. The training and test ROC curves of RF classifier are shown in Fig. 3. The area under the curve (AUC) of an ROC curve provides another measure for the classification performance. The larger the AUC, the better the performance. An AUC of 98.2 per cent is obtained for the test ROC.

Using the prediction model with the best threshold obtained from the test ROC curve in Fig. 3, we run the PSR/NON_PSR classification on the 200 unidentified/unassociated sources. 27 of them have been classified as PSR by our model. We summarize their properties in Table 3, which includes their names in 3FHL catalogue, γ-ray positions and errors, the corresponding name in 3FGL catalogue (if there is any), and the confidence score of belonging to PSR class assigned by our model. The confidence score for a given source provides a gauge for the reliability of the class assignment as predicted by the model, which should not be interpreted as the probability of the source as a PSR. The distributions of these 27 selected PSR candidates in the projected feature spaces are shown by the black triangles in Fig. 2. Except for two outliers (3FHL J1915.2–1323 and 3FHL J0737.5+6534) with
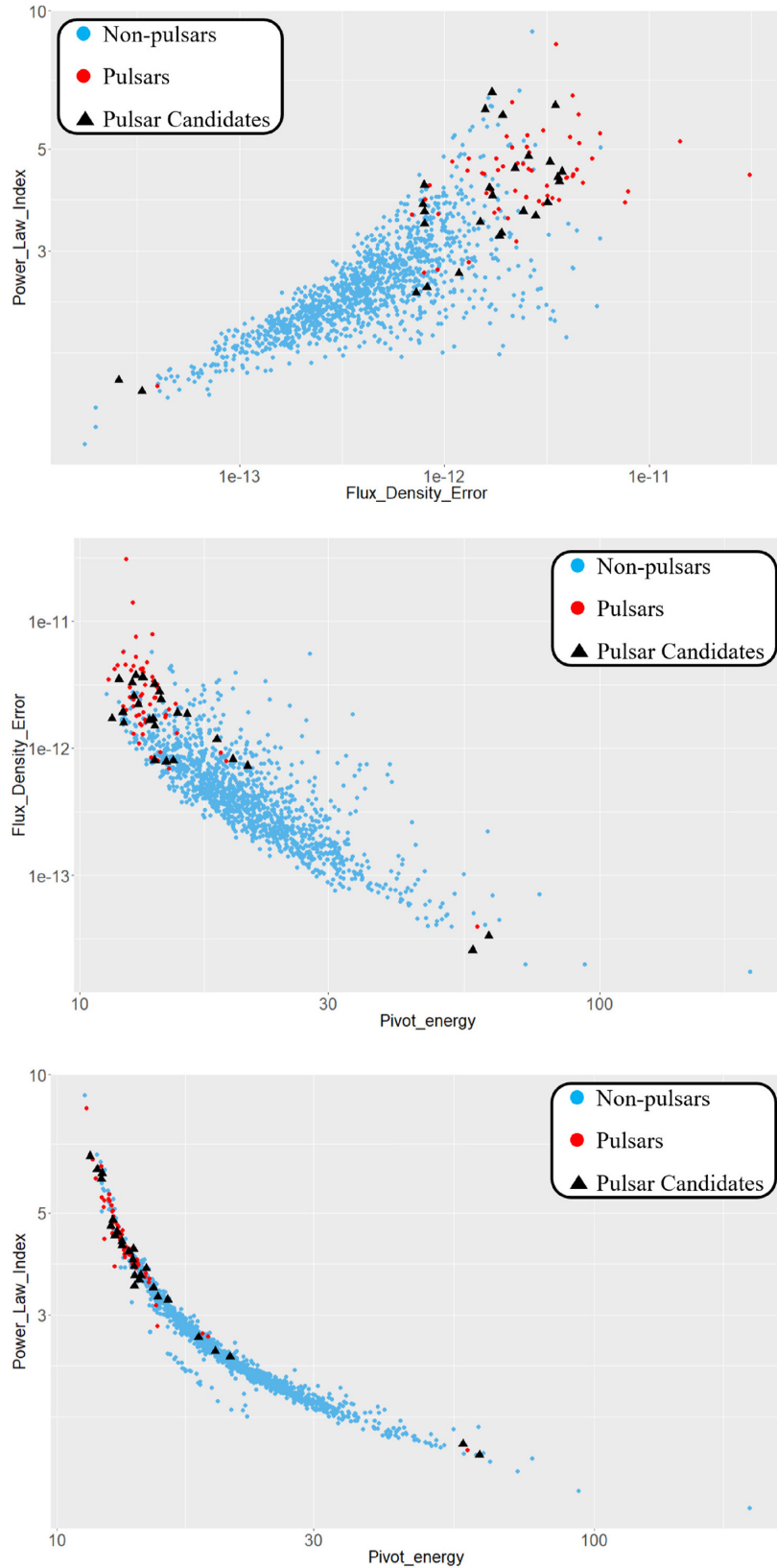
Figure 2. Two-dimensional projections of feature space for the selected features of high importance scores. The red dots and the blues dots show the distributions of known PSR sources and NON_PSR sources in 3FHL catalogue, respectively. The black triangles represent the PSR candidates selected by our scheme.

Table 2. The accuracies of seven prediction models for the 3FHL catalogue as evaluated by the test set.

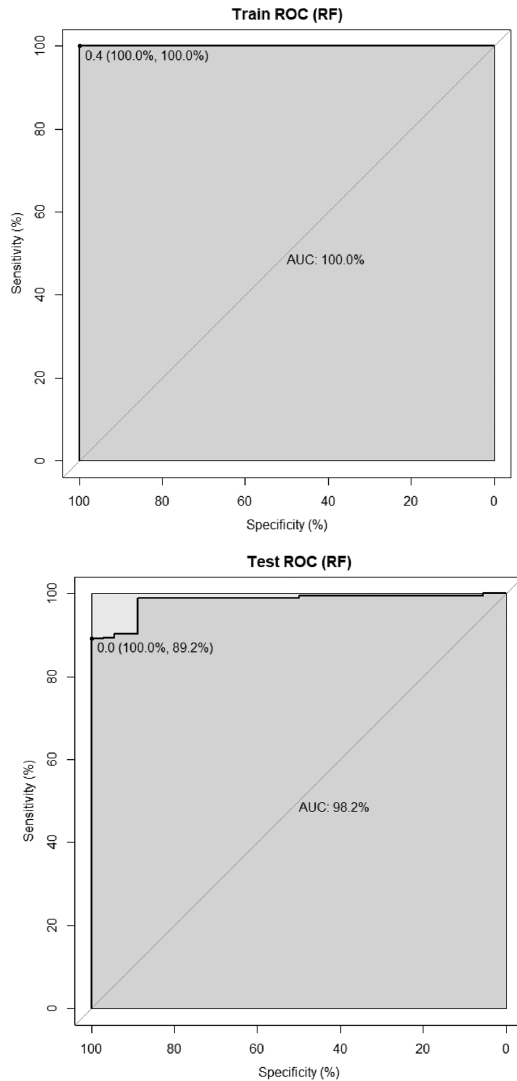| Classifiers	Our framework
RF	**98.03%**
Boost LR	97.78%
LR	97.54%
GAM	95.82%
SVM	97.54%
DT	93.31%
LMT	94.59%

Figure 3. The training and test ROC curves produced by random forest (RF) classifier using 3FHL catalogue.

low PSR confidence scores, other candidates are clustered in the regime occupied by the known pulsars in 3FHL catalogue.

Kaur et al. (2019) have reported 36 unidentified 3FHL sources that most likely belong to AGNs family. In comparing their list (table 4 in their paper) with our PSR candidate list, only one source 3FHL J0541.1–4855, which has a relatively low PSR confidence score of 0.166, is overlapped. This provides further confidence for our method and the PSR candidates selected by this scheme.

3 DATA ANALYSIS

3.1 Searching for X-ray/optical sources within the γ-ray error ellipses

We have searched for X-ray counterparts associated with our shortlisted 3FHL sources by using archival X-ray spectral imaging data. We attempted to detect the X-ray sources within the γ-ray error ellipses of these candidates with a wavelet detection algorithm. Only the X-ray sources detected at a significance larger than 4σ are considered as genuine in our work. Among 27 PSR-like candidates in Table 3, 10 of them have X-ray sources found within their 95 per cent confidence γ-ray error ellipses. The results are summarized in Table 4. X-ray images of the fields of these 10 PSR-like candidates are shown in Fig. 4.

We found that these selected candidates have been observed either by *Chandra*, *XMM–Newton*, or *Swift*. If *Chandra* data are available for a PSR-like candidate, we solely used its data to determine the positions of the X-ray counterparts as *Chandra* can provide the best positional accuracy among all X-ray telescopes. For the cases there is no archival *Chandra* data but with *XMM–Newton* available, the positions of the X-ray counterparts are determined by the MOS cameras (merged MOS1/2 data) because their pixel size provides a full sampling of the point spread function of the mirror. For *Swift* XRT observations, we noticed that their exposures are typically a few ks that are unconstraining for our searches of relatively faint sources potentially associated with pulsars. Therefore, the observations by *Swift* XRT have ignored in this work.

By assuming an absorbed power law with a photon index of $\Gamma_X = 2$ and the column absorption n_H adopted at the value of the Galactic H I column density in the directions towards these X-ray sources (Kalberla et al. 2005), with the aid of PIMMS (version 4.9a), we systematically computed the absorption-corrected X-ray fluxes F_X for all the X-ray sources in an energy range of 0.3–10 keV by using their count rates. Hence, we obtained their X-ray to γ-ray flux ratios F_X/F_γ with F_γ as the energy flux in 10 GeV to 2 TeV as obtained from 3FHL catalogue. F_X and F_X/F_γ are summarized in columns 8 and 9 in Table 4.

In Fig. 5, we compare the distributions of $\log F_X/F_\gamma$ of these X-ray sources with those of the known pulsars in the same energy ranges. The range of $\log F_X/F_\gamma$ spanned by these X-ray sources is bracketed by those of the known pulsars, except for two sources J18007_X8 and J17472_X8 that have the lowest $\log F_X/F_\gamma$.

We have also examined the temporal variability of these X-ray sources. We first search for the short-term variability within each observation window by using the Gregory–Loredo variability algorithm (Gregory & Loredo 1992). By testing whether the arrival times of these sources are uniformly distributed, only J18007_X1 has a probability of > 90 per cent as a variable source.

Apart from the short-term variabilities, a number of X-ray sources have been observed more than once. These multi-epoch X-ray data allow us to further examine their long-term flux variability. We compare the difference of the fluxes with their errors combined by quadrature, i.e. $|F_{obs1} - F_{obs2}| / \sqrt{\sigma_{obs1}^1 + \sigma_{obs1}^2}$. The largest difference found for each source is summarized in the column 10 in Table 4. We consider a source to have long-term variability if the maximal difference of its flux in two observations is larger than 4σ. Four sources, J17472_X5, J0737_X1, J0737_X2, and J0737_X5, are found to be significantly variable. For those with non-detection in certain epoch(s), we have placed lower bounds on their long-term variabilities instead.

Table 3. 27 PSR candidates selected from 3FHL catalogue. θ_{95} are their γ-ray positional uncertainty at the 95 per cent confidence level.

3FHL name	RA (J2000) (ʰ ᵐ ˢ)	Dec. (J2000) (° ′ ″)	θ_{95} (°)	3FGL name	PSR confidence score
3FHL J1748.6–2816	17 48 38.4	–28 16 41	0.035	3FGL J1748.3–2815c	0.858
3FHL J1839.4–0553	18 39 24.3	–05 53 46	0.040	3FGL J1839.3–0552	0.852
3FHL J1823.3–1339	18 23 21.7	–13 39 46	0.031	3FGL J1823.2–1339	0.84
3FHL J1748.1–2903	17 48 08.9	–29 03 42	0.039	3FGL J1747.7–2904	0.79
3FHL J1139.2–6248	11 39 16.7	–62 48 09	0.044	3FGL J1139.0–6244	0.768
3FHL J1857.0+0059	18 57 05.7	+00 59 23	0.058	3FGL J1857.2+0059	0.668
3FHL J1753.8–2537	17 53 48.1	–25 37 46	0.026	3FGL J1754.0–2538	0.66
3FHL J1802.3–3043	18 02 23.7	–30 43 20	0.049	3FGL J1802.4–3043	0.658
3FHL J1907.0+0713	19 07 00.6	+07 13 43	0.046	...	0.602
3FHL J1800.7–2357	18 00 44.1	–23 57 12	0.051	3FGL J1800.8–2402	0.59
3FHL J1603.3–6011	16 03 22.9	–60 11 59	0.048	3FGL J1603.7–6011	0.522
3FHL J1855.5+0142	18 55 35.8	+01 42 55	0.047	...	0.516
3FHL J1405.1–6118	14 05 06.2	–61 18 06	0.034	3FGL J1405.1–6119	0.466
3FHL J1306.3–6042	13 06 22.5	–60 42 39	0.028	3FGL J1306.4–6043	0.45
3FHL J1626.3–4915	16 26 23.9	–49 15 23	0.076	3FGL J1626.2–4911	0.418
3FHL J1112.5–6054	11 12 33.5	–60 54 40	0.072	3FGL J1111.9–6058	0.4
3FHL J1747.2–2822	17 47 17.7	–28 22 00	0.033	...	0.372
3FHL J1824.3–0621	18 24 18.0	–06 21 05	0.045	3FGL J1824.3–0620	0.364
3FHL J0725.6–5008	07 25 39.1	–50 08 25	0.043	3FGL J0725.4–5007	0.334
3FHL J0541.1–4855	05 41 10.7	–48 55 43	0.072	...	0.166
3FHL J1915.2–1323	19 15 16.4	–13 23 30	0.051	...	0.162
3FHL J0737.5+6534	07 37 35.3	+65 34 43	0.033	...	0.158
3FHL J1657.6–4656	16 57 37.1	–46 56 54	0.095	3FGL J1657.6–4653	0.144
3FHL J1803.1–6709	18 03 10.7	–67 09 49	0.053	3FGL J1803.3–6706	0.142
3FHL J1200.3+0201	12 00 22.7	+02 01 44	0.061	3FGL J1200.4+0202	0.132
3FHL J0110.9+4346	01 10 56.5	+43 46 54	0.082	...	0.124
3FHL J0115.4–2916	01 15 24.2	–29 16 57	0.055	...	0.118

Since the X-ray data provide much better constraints on the positions of the potential counterparts, we are able to search for the possible optical/infrared (IR) counterparts of these X-ray sources. We searched the following optical and (near)IR source catalogues for the counterpart to the X-ray sources (search radius = 1 arcsec): the Panoramic Survey Telescope and Rapid Response System (Pan-STARRS) DR2 (PS1; Chambers et al. 2016), Galactic Legacy Infrared Mid-Plane Survey Extraordinaire (GLIMPSE; Spitzer Science Center 2009), the *Spitzer* point-source catalogue of seven nearby galaxies (Khan et al. 2015), VISTA Variables in the Via Lactea (VVV; Saito et al. 2012; Minniti et al. 2017), *Wide-field Infrared Survey Explorer* (*WISE*) all-sky catalogue (Cutri et al. 2012), and *Gaia* Data Release 2 (DR2; Gaia Collaboration et al. 2018). Most of the 3FHL sources are close to the Galactic plane with heavy extinction, and several (near)IR catalogues were thus used. For every optical counterpart, we made an extinction-corrected spectral energy distribution (SED) and fit it with the blackbody model. Dereddening was done using the extinction curve of Fitzpatrick (1999) with an extinction value (A_v) inferred from the hydrogen column density in the X-ray analysis (i.e. $N_H/A_v = 2.21 \times 10^{21}$; Güver & Özel 2009).

Table 5 shows the SED fitting results. Except for those have *Gaia* distance measurements (Bailer-Jones et al. 2018), a distance of 1 kpc is assumed for the calculations of the blackbody radii (the radius is proportional to the distance). As mentioned, most of the sources are highly absorbed and therefore their SEDs are largely affected by the dereddening. Given that the extinctions adopted are full Galactic values, the SEDs of some nearby sources (e.g. J16263_X2) could be overcorrected and appear to be much bluer than they should be.

Undercorrection is also possible if a source is with high intrinsic absorption.

3.2 Detailed analysis of individual PSR-like candidates

The details of the X-ray observations and data analyses of these 10 PSR candidates are given in the followings.

3.2.1 3FHL J1748.6–2816

Both *Chandra* (Obs ID: 2269) and *XMM–Newton* (Obs ID: 0694641401) have observed the field of 3FHL J1748.6–2816 on 2001 July 16 and 2012 September 30 for the effective exposures of 18 and 32 ks, respectively. In both observations, only one X-ray source is detected within the γ-ray positional error ellipse that is denoted as J17486_X1 (see Fig. 4). Searching in SIMBAD data base, we found the nature of this source remains to be unidentified. For estimating its absorption-corrected X-ray flux as given in Table 4, we adopted the count rate from the *Chandra* observation and assumed a column absorption of $n_H = 1.3 \times 10^{22}$ cm^{-2} at the same level as the Galactic H I column density in the corresponding direction (Kalberla et al. 2005).

Besides J17486_X1, there are other sources are detected serendipitously in the whole field of view (FoV) covered by the cameras in both observations. We have considered the possibility that one or more sources lie within the error ellipse by chance. We counted the number of X-ray sources detected in the whole FoV and computed the source density. Based on this, we estimated the number of chance coincidences λ expected within the γ-ray error ellipse. Assuming a Poisson distribution, the probability of finding one or more chance

Table 4. Properties of X-ray sources within γ-ray error ellipses (95 per cent confidence) of selected 3FHL unidentified objects.

Source	RA (J2000) (h m s)	Dec (J2000) (° ′ ″)	σ_{pos} (arcsec)	Signifi. (σ)	Inst.	Count rate (10^{-3} counts s^{-1})	$F_{0.3-10\,keV}^{unabs}$ (10^{-14} erg cm^{-2} s^{-1})	F_X/F_γ (10^{-3})	Variability (S/L)
				3FHL J1748.6–2816					
J17486_X1	17:48:40.85	−28:18:22.80	0.47	6.86	C*, X	1.45 ± 0.36	6.09 ± 1.51	$15.20_{-5.88}^{+9.32}$	N/2.4σ
				3FHL J1839.4–0553					
J18394_X1	18:39:19.12	−05:54:06.73	0.34	9.68	C*	1.56 ± 0.30	$7.69_{-1.53}^{+1.48}$	$20.17_{-7.26}^{+11.99}$	N/1.4σ
J18394_X2	18:39:21.02	−05:53:28.23	0.41	7.93	C*	1.35 ± 0.29	$6.65_{-1.38}^{+1.43}$	$17.46_{-6.41}^{+10.9}$	N/
				3FHL J1823.3–1339					
J18233_X1	18:23:19.80	−13:40:09.90	0.58	7.43	X*	5.06 ± 0.84	$19.82_{-3.29}^{+3.25}$	$34.23_{-10.41}^{+15.49}$	N/
				3FHL J1748.1–2903					
J17481_X1	17:48:04.36	−29:02:27.97	0.30	4.02	C*	0.28 ± 0.09	$1.14_{-0.37}^{+0.36}$	$5.22_{-2.50}^{+4.65}$	N/>2.9σ
J17481_X2	17:48:05.67	−29:04:05.09	0.16	8.05	C*	1.33 ± 0.35	5.40 ± 1.42	$24.77_{-10.75}^{+20.02}$	N/>2.0σ
				3FHL J1857.0+0059					
J18570_X1	18:57:13.48	+01:01:46.54	0.45	6.63	X*	0.68 ± 0.19	2.09 ± 0.57	$6.65_{-2.84}^{+4.92}$	N/
				3FHL J1800.7–2357					
J18007_X1	18:00:36.99	−23:55:55.90	0.22	6.46	C*	0.34 ± 0.08	1.36 ± 0.30	$3.51_{-1.43}^{+2.71}$	Y/
J18007_X2	18:00:33.80	−23:57:38.24	0.37	5.91	C*	0.25 ± 0.06	1.00 ± 0.25	$2.58_{-1.10}^{+2.09}$	N/
J18007_X3	18:00:49.51	−23:59:41.61	0.34	5.42	C*	0.27 ± 0.07	1.09 ± 0.27	$2.80_{-1.20}^{+2.27}$	N/
J18007_X4	18:00:41.89	−23:56:48.43	0.52	5.24	C*	0.28 ± 0.07	1.11 ± 0.28	$2.86_{-1.23}^{+2.34}$	N/
J18007_X5	18:00:32.56	−23:58:22.45	0.34	5.09	C*	0.23 ± 0.06	0.93 ± 0.25	$2.40_{-1.06}^{+2.01}$	N/
J18007_X6	18:00:36.88	−23:59:24.06	0.22	5.01	C*	0.21 ± 0.06	0.82 ± 0.23	$2.12_{-0.95}^{+1.80}$	N/
J18007_X7	18:00:44.13	−23:57:51.04	0.31	4.35	C*	0.20 ± 0.06	0.79 ± 0.24	$2.04_{-0.95}^{+1.79}$	N/
J18007_X8	18:00:35.67	−23:57:50.23	0.34	4.13	C*	0.16 ± 0.05	0.65 ± 0.21	$1.68_{-0.81}^{+1.53}$	N/
				3FHL J1405.1–6118					
J14051_X1	14:05:14.45	−61:18:27.63	0.10	23.92	C*	5.32 ± 0.65	27.09 ± 3.31	$48.29_{-18.03}^{+42.19}$	N/
J14051_X2	14:05:06.47	−61:16:23.56	0.38	7.47	C*	1.48 ± 0.35	7.54 ± 1.80	$13.43_{-6.11}^{+14.30}$	N/
				3FHL J1626.3–4915					
J16263_X1	16:26:01.95	−49:14:11.29	0.35	11.77	C*, X	6.63 ± 0.93	$33.76_{-4.74}^{+4.73}$	$66.46_{-26.37}^{+65.36}$	N/2.0σ
J16263_X2	16:26:29.28	−49:15:43.69	0.33	8.94	C*	2.32 ± 0.50	12.12 ± 2.61	$23.86_{-10.72}^{+26.59}$	N/>3.7σ
J16263_X3	16:26:08.53	−49:17:44.38	0.55	6.36	X*	4.64 ± 1.06	$20.44_{-4.63}^{+4.66}$	$40.24_{-18.40}^{+45.72}$	N/
				3FHL J1747.2–2822					
J17472_X1	17:47:20.91	−28:23:04.49	0.36	9.35	C*, X	0.90 ± 0.13	$3.73_{-0.53}^{+0.52}$	$6.65_{-2.42}^{+4.96}$	N/3.1σ
J17472_X2	17:47:22.41	−28:23:26.38	0.33	6.47	C*	0.47 ± 0.09	1.93 ± 0.38	$3.44_{-1.39}^{+2.87}$	N/3.3σ
J17472_X3	17:47:09.34	−28:21:37.01	0.32	6.18	C*	0.47 ± 0.09	1.87 ± 0.38	$3.34_{-1.36}^{+2.81}$	N/>2.6σ
J17472_X4	17:47:09.33	−28:21:55.24	0.26	5.76	C*	0.43 ± 0.09	1.74 ± 0.37	$3.10_{-1.29}^{+2.66}$	N/>2.4σ
J17472_X5	17:47:14.27	−28:21:09.82	0.51	5.11	C*	0.34 ± 0.08	1.62 ± 0.33	$2.89_{-1.18}^{+2.44}$	N/4.3σ
J17472_X6	17:47:13.07	−28:23:22.76	0.23	4.30	C*	0.30 ± 0.08	1.22 ± 0.32	$2.18_{-0.99}^{+2.05}$	N/2.5σ
J17472_X7	17:47:20.50	−28:23:46.16	0.36	4.28	C*	0.37 ± 0.10	1.53 ± 0.40	$2.72_{-1.23}^{+2.55}$	N/>1.8σ
J17472_X8	17:47:23.80	−28:22:30.27	0.45	4.02	C*	0.21 ± 0.06	0.88 ± 0.26	$1.57_{-0.74}^{+1.54}$	N/>1.5σ
				3FHL J0737.5+6534					
J07375_X1	07:37:33.39	+65:33:07.54	0.07	71.24	C*, X	6.30 ± 0.36	10.16 ± 0.58	$55.22_{-24.80}^{+147.42}$	N/12.2σ
J07375_X2	07:37:40.49	+65:35:21.72	0.08	33.45	C*, X	2.30 ± 0.22	$3.72_{-0.34}^{+0.35}$	$20.2_{-9.48}^{+56.62}$	N/8.1σ
J07375_X3	07:37:52.85	+65:34:07.68	0.23	10.45	C*	0.66 ± 0.12	$1.06_{-0.19}^{+0.20}$	$5.78_{-3.02}^{+17.96}$	N/>3.8σ
J07375_X4	07:37:36.50	+65:32:51.04	0.17	5.55	C*	0.37 ± 0.10	0.60 ± 0.15	$3.25_{-1.84}^{+10.95}$	N/>2.1σ
J07375_X5	07:37:38.37	+65:36:29.32	0.33	5.03	C*, X	0.27 ± 0.08	0.44 ± 0.13	$2.36_{-1.38}^{+8.22}$	N/4.0σ
J07375_X6	07:37:17.94	+65:35:09.74	0.33	4.48	C*	0.27 ± 0.08	0.43 ± 0.13	$2.36_{-1.40}^{+8.31}$	N/>2.3σ
J07375_X7	07:37:35.25	+65:35:50.00	0.15	4.20	C*	0.25 ± 0.08	0.40 ± 0.13	$2.18_{-1.31}^{+7.78}$	N/>2.3σ
J07375_X8	07:37:43.71	+65:33:45.70	0.20	4.12	C*	0.28 ± 0.09	0.46 ± 0.14	$2.48_{-1.48}^{+8.79}$	N/>2.3σ

Note. The chance coincidence can be seen next to the 3FHL name. An asterisk symbol ($*$) means that the coordinate and significance are extracted. For whole analysis, we used the WAVDETECT task in CIAO. The count rate was calculated from the net_counts for $*$'s instrument with exposure time.
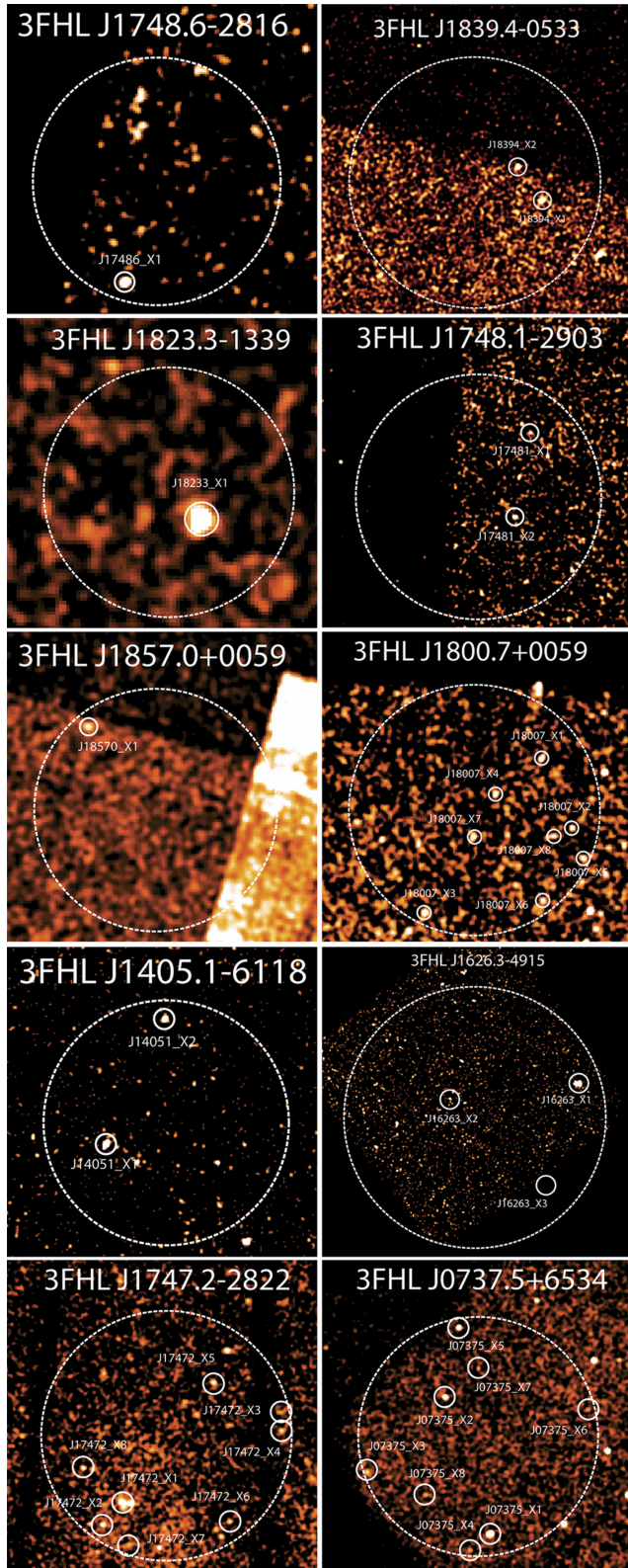
Figure 4. X-ray sources (solid circles) found within the 95 per cent γ-ray positional error ellipses (dashed ellipses) of our selected PSR-like 3FHL sources. Top is north and left is east in all images.
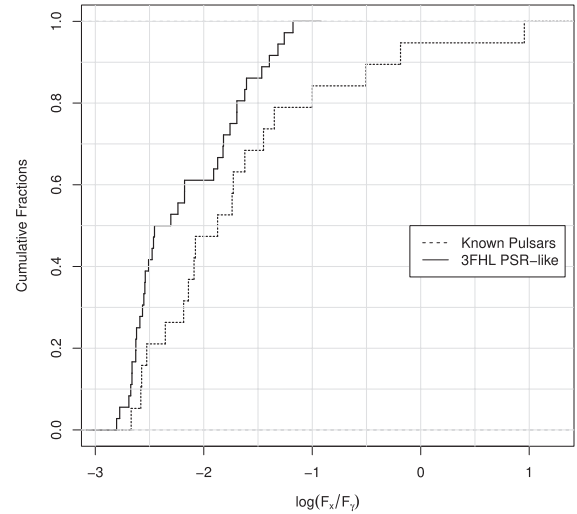
Figure 5. Comparison for the distributions of $\log F_X/F_\gamma$ of known pulsars in 3FHL and the sources in Table 4. The fluxes in X-ray and γ-ray are evaluated in 0.3–10 keV and 10 GeV–2 TeV, respectively.

coincidences of X-ray sources is given by

$$P\,(n \geq 1) = \sum_{n=1}^{\infty} \frac{\lambda^n \, e^{-\lambda}}{n!} = 1 - e^{-\lambda}. \tag{1}$$

For 3FHL J1748.6–2816, we found that $P\,(n \geq 1) \sim 40$ and ~ 34 per cent in *Chandra* and *XMM–Newton* observations, respectively. J17846_X1 does not show any X-ray flux variability either in individual observations or between two observations at different epoch. Optical/IR counterpart of J17846_X1 has been identified. A blackbody fit to its extinction-corrected SED yields a temperature of $T_{bb} \sim 1.2 \times 10^4$ K and an emitting region with a radius of $R_{bb} \sim 1.3 d_{kpc}$ R$_\odot$ (cf. Table 5), where d_{kpc} is the distance at unit of 1 kpc.

In this work, a detailed X-ray spectral fitting will be carried out for those sources with more than 50 net counts detected. The results are summarized in Table 6. Since the net counts of J17486_X1 collected from both observations is ∼140 counts, we have extracted its spectrum and fitted with both absorbed power-law model and absorbed blackbody model. Both models result in a similar goodness of fit. The best-fitting power law yields a column absorption of $n_H = 1.3^{+0.7}_{-0.5} \times 10^{22}$ cm^{-2}, a photon index of $\Gamma_X = 3.1^{+0.9}_{-0.7}$, and an absorption-corrected of $F_X \sim 2.1 \times 10^{-13}$ erg cm^{-2} s^{-1} in 0.3–10 keV. The best-fitting $\Gamma \sim 3$ appears to be quite steep that indicate the X-ray emission is rather soft. Considering a purely thermal emission scenario, the best-fitting blackbody yields a temperature of $kT = 0.6 \pm 0.1$ keV with an absorption-corrected of $F_X \sim 2.7 \times 10^{-14}$ erg cm^{-2} s^{-1} in 0.3–10 keV. The normalization of the blackbody implies an X-ray emission region with a radius of $\sim 13.4 d_{kpc}$ m.

3.2.2 3FHL J1839.4–0553

The γ-ray error ellipse of 3FHL J1839.4–0553 has been covered by two *Chandra* observations with the Advanced CCD Imaging Spectrometer (ACIS-I) on 2008 March 9 (Obs. ID: 7493) and 2007 November 5 (Obs. ID: 7630) for an effective exposure of 20 and 28 ks, respectively. Within the 95 per cent γ-ray error ellipse, there are two X-ray sources J18394_X1 and J18394_X2 (see Fig. 4).

Table 5. Results of blackbody fits to the optical/IR SED of the possible counterparts associated with the X-ray sources found in the error ellipses of PSR-like 3FHL sources.

Name	Temperature (K)	Radius ($R_\odot$)	Distance[a] (kpc)	Reference magnitude[b]	Extinction (A_v)	Offset (arcsec)
J17486_X1	11 800 ± 1700	1.3 ± 0.2	(1)	16.9 (0.62 μm)	5.9	0.8
J18007_X2	1400 ± 100	10 ± 2	(1)	17.6 (1.0 μm)	5.3	0.5
J18007_X3	3000 ± 300	3.1 ± 0.4	(1)	13.0 (2.2 μm)	5.3	0.9
J18007_X5	21 100 ± 7600	0.20 ± 0.05	0.9	20.1 (0.49 μm)	5.3	0.4
J18007_X6	1300 ± 200	5.6 ± 1.6	(1)	17.1 (1.6 μm)	5.3	0.6
J18007_X8	4700 ± 200	2.4 ± 0.2	2.5	19.8 (0.62 μm)	5.3	0.3
J14051_X1	2031 ± 155	6.6 ± 0.7	(1)	14.4 (1.7 μm)	8.5	0.5
J14051_X1[c]	40 000 (fixed)	12.9 ± 0.8	7.7	14.4 (1.7 μm)	31.6	0.5
J16263_X1[d]	–	1.1	(1)	19.1 (1.6 μm)	8.9	0.6
J16263_X2[d]	–	–	3.6	19.0 (0.51 μm)	8.9	0.4
J17472_X8	1900 ± 200	11 ± 2	(1)	13.3 (1.7 μm)	5.7	0.4
J07375_X1	800 ± 300	4.0 ± 2.6	(1)	15.8 (3.6 μm)	0.20	0.4
J07375_X2	900 ± 100	1.3 ± 0.2	(1)	17.4 (3.6 μm)	0.20	0.1
J07375_X3	5800 ± 200	0.18 ± 0.01	1.6	18.9 (0.49 μm)	0.18	0.6
J07375_X4	1000 ± 300	0.60 ± 0.33	(1)	18.7 (3.6 μm)	0.19	0.7
J07375_X6	4000 ± 600	0.15 ± 0.04	(1)	20.9 (0.62 μm)	0.23	0.4
J07375_X8	2300 ± 100	0.78 ± 0.05	(1)	21.4 (0.62 μm)	0.19	0.3

[a]Unless a *Gaia* distance is found, $d = 1$ kpc is assumed.
[b]Observed magnitudes of the shortest wavelength (in the brackets) that can be found in the aforementioned catalogues.
[c]Distance and the extinction are adopted from Corbet et al. (2019).
[d]Only two data points in the SED and therefore no uncertainty can be obtained.

Table 6. X-ray spectral properties of X-ray sources with more than 50 net counts collected from the archival data. The results from both power-law fits and blackbody fits are summarized. The quoted uncertainties are 1σ for one parameter of interest.

Name	Power-law fit				Blackbody fit			
	n_H (10^{22} cm)	Γ_X	χ^2/dof	$F^{unabs}_{0.3-10\,keV}$ (erg cm^{-2} s^{-1})	n_H (10^{22} cm)	kT (keV)	χ^2/dof	$F^{unabs}_{0.3-10\,keV}$ (erg cm^{-2} s^{-1})
J17486_X1	$1.3^{+0.7}_{-0.5}$	$3.1^{+0.9}_{-0.7}$	20.42/32	$2.1 \pm 0.2 \times 10^{-13}$	$0.23^{+0.35}_{-0.22}$	$0.61^{+0.12}_{-0.11}$	19.43/32	$2.7 \pm 0.3 \times 10^{-14}$
J18394_X1	≤2.6	$0.02^{+0.77}_{-0.54}$	5.53/10	$6.4 \pm 1.0 \times 10^{-14}$	≤1.8	$2.6^{+2.9}_{-0.9}$	5.80/10	$5.3 \pm 0.8 \times 10^{-14}$
J18233_X1	$1.9^{+0.8}_{-0.6}$	1.1 ± 0.3	38.55/40	$2.8^{+0.9}_{-0.5} \times 10^{-13}$	$0.44^{+0.37}_{-0.27}$	1.8 ± 0.2	38.33/40	$2.0 \pm 0.2 \times 10^{-13}$
J18570_X1	$3.0^{+1.8}_{-1.3}$	$1.3^{+0.7}_{-0.6}$	15.80/23	$5.8 \pm 0.7 \times 10^{-14}$	$1.3^{+1.1}_{-0.7}$	$1.6^{+0.6}_{-0.4}$	17.91/23	$3.6 \pm 0.4 \times 10^{-14}$
J14051_X1	$15.0^{+8.0}_{-5.0}$	$2.7^{+1.4}_{-1.1}$	13.97/21	$2.4^{+53.2}_{-1.9} \times 10^{-12}$	$9.2^{+5.1}_{-3.4}$	$1.3^{+0.4}_{-0.3}$	13.71/21	$3.0^{+1.4}_{-0.7} \times 10^{-13}$
J16263_X1	$0.65^{+1.03}_{-0.65}$	$2.0^{+0.7}_{-0.6}$	16.31/23	$2.7^{+3.8}_{-0.9} \times 10^{-13}$	≤0.34	0.90 ± 0.10	15.78/23	$1.2 \pm 0.2 \times 10^{-13}$
J16263_X3	$0.84^{+0.24}_{-0.20}$	$4.0^{+0.7}_{-0.6}$	10.51/23	$1.9 \pm 0.2 \times 10^{-12}$	$0.16^{+0.19}_{-0.15}$	$0.40^{+0.07}_{-0.06}$	13.16/23	$1.2 \pm 0.1 \times 10^{-13}$

J18394_X1 has been detected by both observations. Therefore, we are able to estimate its long-term variability that is only at 1.4σ level. On the other hand, J18394_X2 is out of the FoV in one *Chandra* observation (Obs. ID: 7630). The nature of both X-ray sources is not known. Their absorption-corrected X-ray fluxes as given in Table 4 is estimated by assuming a column absorption of $n_H = 1.8 \times 10^{22}$ cm^{-2}, which is consistent with the total Galactic H I absorption at that direction, with the count rates observed by Obs. ID: 7493. Taking all the X-ray sources detected in the entire FoV in the observation, $P(n \geq 1)$ is found to be ∼65 per cent. Searching for their counterparts in other wavelengths with the archival data does not yield any positive result.

J18394_X1 has ∼58 net counts collected from both observations and therefore we have further examined its X-ray spectrum (see Table 6). Its X-ray spectrum appears to be rather flat in the energy range of 0.5–8 keV. Both power-law and blackbody fits suggest the column absorption can be lower than that inferred from the Galactic H I absorption. The best-fitting power law yields $n_H < 2.6 \times 10^{22}$ cm^{-2}, $\Gamma_X = 0.02^{+0.77}_{-0.54}$, and $F_X \sim 6.4 \times 10^{-14}$ erg cm^{-2} s^{-1} in 0.3–10 keV. On the other hand, the best-fitting blackbody yields $n_H < 1.8 \times 10^{22}$ cm^{-2}, $kT = 2.6^{+2.9}_{-0.9}$ keV, and $F_X \sim 5.3 \times 10^{-14}$ erg cm^{-2} s^{-1} in 0.3–10 keV.

3.2.3 3FHL J1823.3–1339

3FHL J1823.3–1339 has been observed by *XMM–Newton* on 23 March 2002 (Obs. ID: 0040140201) for an effective exposure of ∼11 ks. Only one single X-ray source, J18233_X1, is detected within its γ-ray error ellipse. Its X-ray image as observed by MOS1/2 camera on-board *XMM–Newton* is displayed in Fig. 4. Using the serendipitous X-ray sources detected in the FoV of MOS camera, the probability of finding an X-ray source within the error ellipse of 3FHL J1823.3–1339 is found to be $P(n \geq 1) \sim$ 12 per cent, which is the lowest among all the selected 3FHL PSR-like candidates in this work. We noticed that the feature is apparently extended with an angular size of ∼30 arcsec and has the peak emission located at RA (J2000) = $18^h23^m19^s$, Dec. (J2000) = $-13°40'02''$. This extended X-ray feature is identified for the first time. A close-up view of J18233_X1 is shown in the right-hand panel of Fig. 6.
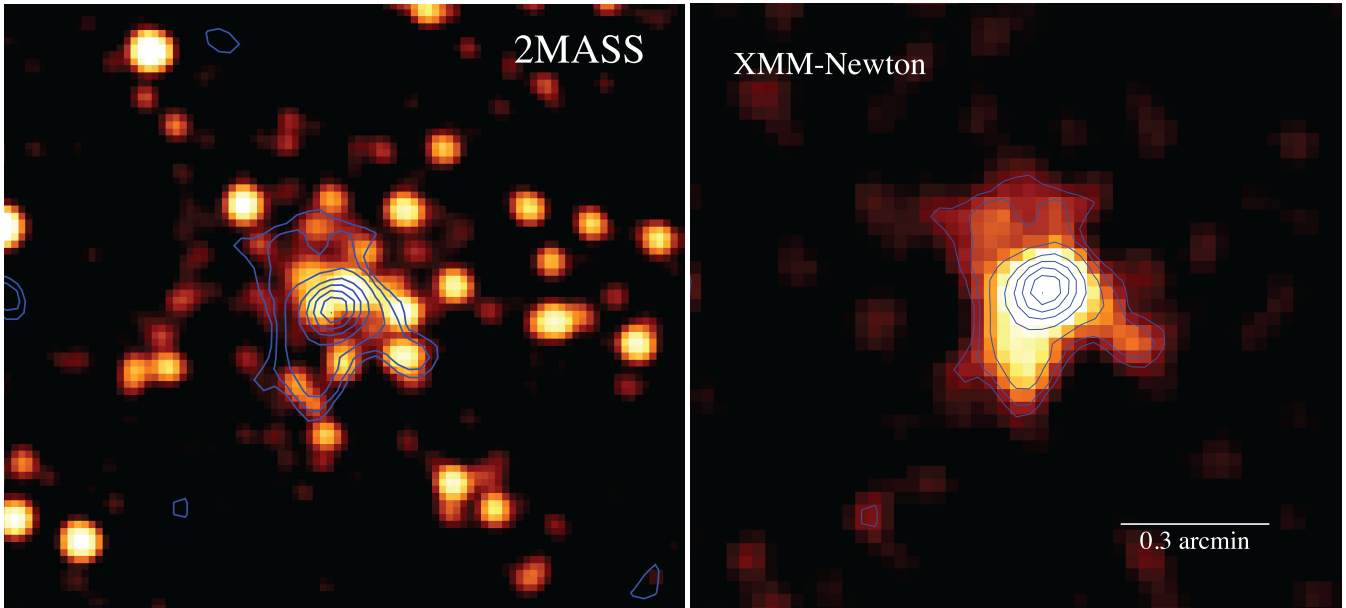
Figure 6. Left-hand panel: K_s-band image of a field centred at Mercer 5 obtained by the Two Micron All-Sky Survey (2MASS). A central concentration of stars can be noted. Right-hand panel: X-ray image of J18233_X1 in 0.3–10 keV with data from MOS1 and MOS2 on-board *XMM–Newton* combined. This is the only X-ray source lies within the γ-ray error ellipse of 3FHL J1823.3–1339. An apparently extended X-ray feature is discovered at the location of Mercer 5. We overlay the X-ray contours on the IR image for comparing the morphology at different wavelengths. Top is north and left is east.

Searching for the nature of this extended source in SIMBAD data base, we found that it is possibly associated with a poorly studied globular cluster Mercer 5, which is discovered in the GLIMPSE Survey (Mercer et al. 2005). It is highly obscured in optical regime as it resides in a region of high visual extinction, $A_V \sim 8.5$–12.5 mag (Longmore et al. 2011), which suggests an X-ray absorption at the level of $(1.2$–$2.8) \times 10^{22}$ cm^{-2} (Güver & Özel 2009). In left-hand panel of Fig. 6, we compare the X-ray morphology of J18233_X1 with the K_s-band 2MASS image of Mercer 5 by overlaying the X-ray contours on the IR image. The distribution of the stars in Mercer 5 is comparable with the morphology of J18233_X1. The peak of the X-ray emission coincides with the region with highest stellar density.

The net counts of J18233_X1 collected from all the European Photon Imaging Cameras (EPICs) on the *XMM–Newton* (MOS1/2+PN) is 322 counts. This enables us to carry out a detailed analysis. In examining its X-ray spectrum, we found that it can be well described by an absorbed power-law model with a goodness of fit of $\chi^2 = 38.55$ for 40 dof. The observed X-ray spectra of J18233_X1 and the best-fitting power-law model are displayed in Fig. 7. The X-ray emission of J18233_X1 is quite hard. The best fit yields a column absorption of $n_H = 1.9^{+0.8}_{-0.6} \times 10^{22}$ cm^{-2}, a photon index of $\Gamma_X = 1.1 \pm 0.3$, and an absorption-corrected flux in 0.3–10 keV of $F_X \sim 3 \times 10^{-13}$ erg cm^{-2} s^{-1}. The X-ray column absorption inferred from the spectral fit is consistent with that deduced from the n_H–A_v correlation. This suggests that J18233_X1 and Mercer 5 are very likely to be located at the same distance from us.

We have also attempted to search for X-ray periodicity from J18233_X1. However, we do not find any significant periodic signal from the existing data.

We further investigated if 3FHL J1823.3–1339 can also be the γ-ray counterpart of Mercer 5. 3FHL J1823.3–1339 is also identified in the 3FGL catalogue with designation 3FGL 1823.2–1339 (Acero et al. 2015). In 0.1–100 GeV, its energy flux is $f_\gamma = (9.3 \pm 0.8) \times$
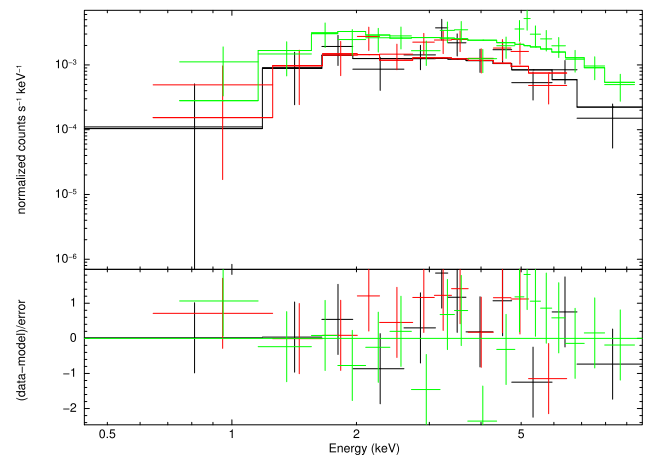

Figure 7. The X-ray spectra of J18233_X1 that is positionally coincident with the globular cluster Mercer 5 as observed by *XMM–Newton* (MOS1/2+PN) cameras and simultaneously fitted to an absorbed power law (upper panel) and contribution to the fitting residuals (lower panel).

10^{-11} erg cm^{-2} s^{-1}. At a distance of $d \sim 5.5$ kpc as estimated by *Gaia* DR2 (Baumgardt et al. 2019), this corresponds to a γ-ray luminosity of $L_\gamma \sim 3.4 \times 10^{35}$ erg s^{-1}. On the other hand, the metallicity of Mercer 5 is estimated to be [Fe/H] ~ -0.86 (Peñaloza et al. 2015). Using its metallicity, we can estimate the expected L_γ from a globular cluster by using the empirical relation: $\log L_\gamma = (0.6 \pm 0.2)[\text{Fe/H}] + (35.6 \pm 0.2)$ (Hui et al. 2011). This implies that the γ-ray luminosity of Mercer 5 is expected at the order of $\sim 10^{35}$ erg s^{-1}. This is consistent with the observed luminosity within the tolerance of the uncertainties of fitted parameters and L_γ. This suggests the γ-rays from 3FHL J1823.3–1339/3FGL 1823.2–1339 are likely from Mercer 5.

3.2.4 3FHL J1748.1–2903

3FHL J1748.1–2903 has been observed by two *Chandra* observations with ACIS-I CCD array on 2006 October 31 (Obs. ID: 7158) and 2017 July 13 (Obs. ID: 19448) with effective exposures of $\sim$14 and $\sim$45 ks, respectively. Using these data, two sources namely J17481_X1 and J17481_X2 are detected within the γ-ray error ellipse. A merged image is shown in Fig. 4. However, J17481_X1 can only be detected in the 2017 observation and J17481_X2 can only be detected in the 2006 observation. Based on the limiting flux in the corresponding epoch of non-detection, we placed the limits on the long-term variability for J17481_X1 and J17481_X2 as $>2\sigma$ and $>3\sigma$, respectively. Both of them are potentially variable X-ray sources. The absorption-corrected X-ray fluxes of J17481_X1 and J17481_X2 tabulated in Table 4 are estimated with their count rates in the corresponding observation and a total Galactic H I column density of $n_H = 1.1 \times 10^{22}$ cm^{-2}. No optical/IR counterpart was found for these two sources. The net counts for both sources are $<$50 counts and therefore no further analysis will be proceeded.

3.2.5 3FHL J1857.0+0059

3FHL J1857.0+0059 has been observed by *XMM–Newton* (Obs. ID: 0784040201) on 2016 October 13 for an effective exposure of $\sim$37 ks. Within its γ-ray ellipse, only one X-ray source J18570_X1 is detected in this data (cf. Fig. 4). The nature of J18570_X1 remains unidentified in SIMBAD data base. The $P(n \geq 1)$ inferred from this observation is $\sim$40 per cent. The absorption-corrected X-ray flux of J1857_X1 as given in Table 4 is estimated by assuming a total Galactic H I column density of $n_H = 1.1 \times 10^{22}$ cm^{-2}. Searching for its multiwavelength counterpart does not yield any result.

On the other hand, we noted that a pulsar PSR J1857+0057 is lying within the 3FHL error circle. The angular separation between PSR J1857+0057 and J18570_X1 is $\sim$5.5 arcmin. Therefore, there is no association between these two objects. PSR J1857+0057 has a spin-down power of $\dot{E} = 4.7 \times 10^{31}$ erg s^{-1} (Manchester et al. 2005). At a distance of $d \sim 2.5$ kpc as inferred by the dispersion measure of this pulsar, 3FHL J1857.0+0059/3FGL J1857.2+0059 has a luminosity of $L_\gamma \sim 3.6 \times 10^{34}$ erg s^{-1} at energies $>$100 MeV that is three orders of magnitude larger than $\dot{E}$. Therefore, we concluded that PSR J1857+0057 cannot be associated with this γ-ray source.

There are $\sim$85 net counts collected from J18570_X1 in this *XMM–Newton* observation. In examining its X-ray spectrum, we found that a best-fitting power law yields $n_H = 3.0^{+1.8}_{-1.3} \times 10^{22}$ cm^{-2}, $\Gamma_X = 1.3^{+0.7}_{-0.6}$, and $F_X \sim 5.8 \times 10^{-14}$ erg cm^{-2} s^{-1} in 0.3–10 keV. And a best-fitting blackbody yields $n_H = 1.3^{+1.1}_{-0.7} \times 10^{22}$ cm^{-2}, $kT = 1.6^{+0.6}_{-0.4}$ keV, and $F_X \sim 3.6 \times 10^{-14}$ erg cm^{-2} s^{-1} in 0.3–10 keV.

3.2.6 3FHL J1800.7–2357

3FHL J1800.7–2357 has been observed by *Chandra* (Obs. ID: 10997) on 2010 July 30 for an effective exposure of $\sim$80 ks. 3FHL J1800.7–2357/3FGL J1800.8–2402 resides in a region where the supernova remnant (SNR) W28 interacts with a number of surrounding molecular cloud (MC; Aharonian et al. 2008). A complex of TeV emission is found in this field (see Fig. 8). 3FHL J1800.7–2357 apparently coincides with a protrusion at the eastern edge of HESS J1800–240B. This leads us to speculate whether this feature is indeed a distinct source or a part of the γ-rays from the SNR–MC interactions. For investigating this issue, VHE
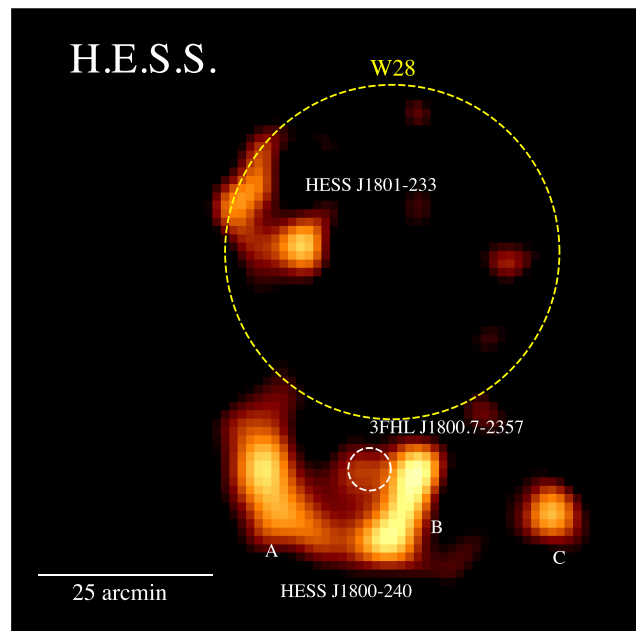

Figure 8. A γ-ray excess map at energies $>$0.1 TeV of the W28 field as obtained by the High Energy Stereoscopic System (H.E.S.S.; Aharonian et al. 2008). Very high energy (VHE) sources HESS J1801–233 and the complex of HESS J1800–240 (regions A, B, and C) can be clearly seen. The location and the angular size of the supernova remnant (SNR) W28 are illustrated by the dotted yellow circle. The dotted white ellipse is the 95 per cent confidence γ-ray positional uncertainty of 3FHL J1800.7–2357.

observation facility with improved spatial resolution is required (e.g. the Cherenkov Telescope Array, CTA).

Cui et al. (2018) have reported an updated analysis of this field with 9-year *Fermi* LAT data. In a 10–200 GeV sky map, they have found features that spatially match HESS J1800–240A, HESS J1800–240B, and HESS J1800–240C. HESS J1800–240B is the brightest among them (fig. 1 in Cui et al. 2018). The GeV spectra of both HESS J1800–240B and HESS J1800–240C show flux discontinuities that suggest there can be several emission components contribute to the γ-rays detected at their locations. While the emission below $\sim$1 GeV can come from the a nearby source with unknown origin, Cui et al. (2018) argue that the γ-rays with energies $\gtrsim$1 GeV from all three spatial components of HESS J1800–240 have a hadronic origin that is dominated by the interactions with the local sea of Galactic cosmic rays.

On the other hand, HESS J1800–240B is potentially associated with a massive star-forming region G5.89–0.39 (Hampton et al. 2016). This suggests finding young neutron stars or pulsars in this region is not unreasonable. However, the high density of X-ray sources in this region makes the probability of having more than one chance coincidence within the error ellipse of 3FHL J1800.7–2357, $P(n \geq 1)$, almost close to 100 per cent. Eight X-ray sources are detected within the γ-ray error ellipse (fig. 4). Total Galactic H I column density of $n_H = 1.2 \times 10^{22}$ cm^{-2} and the count rates of these sources obtained in this observation are adopted for estimating their F_X (cf. Table 4). Based on Gregory–Loredo variability algorithm, J18007_X1 is the only X-ray source in this investigation that shows possible variability in a single observation with a probability $>$ 90 per cent. Its X-ray light curve is shown in Fig. 9. Since the net counts collected from J18007_X1 is $<$50 counts, we do not carry out any further analysis of this source.
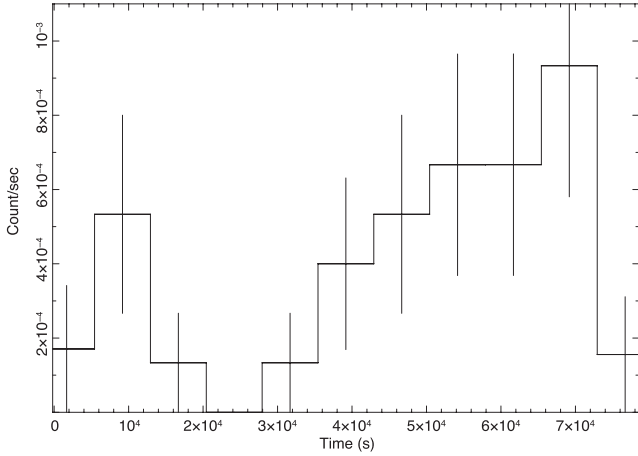
Figure 9. The X-ray light curve of J18007_X1 with a bin size of 7500 s as observed by *Chandra* in 0.3–7 keV.

We have also identified the optical/IR counterparts of J18007_X2, J18007_X3, J18007_X5, J18007_X6, and J18007_X8. By fitting the blackbody model to their SED, temperatures in the range of $T \sim 1300$–$21\,100$ K are yielded (Table 5). For J18007_X5 and J18007_X8, their counterparts can also be found in *Gaia* DR2. Parallax measurements suggest J18007_X5 and J18007_X8 are located at the distance of 0.9 and 2.5 kpc, respectively. Adopting these distances, the blackbody radii of the optical/IR counterparts of J18007_X5 and J18007_X8 are found to be 0.2 and 2.4 $R_\odot$, respectively.

3.2.7 3FHL J1405.1–6118

3FHL J1405.1–6118 has been observed by *Chandra* ACIS-S on 2013 September 19 (Obs. ID: 14888) for an effective exposure of $\sim$13 ks. Two X-ray sources, J14051_X1 and J14051_X2, are detected within the γ-ray error ellipse. The probability of chance coincidence is estimated to be $P\,(n \geq 1) \sim 34$ per cent. Searching in SIMBAD data base, we found that both X-ray sources are unclassified. Their F_X as given in Table 4 are estimated with their detected count rates and a total Galactic H I column density of $n_H = 1.9 \times 10^{22}$ cm^{-2}. J14051_X1 is among the brightest X-ray sources discovered in this work, which is detected at a signal-to-noise ratio (S/N) of $\sim$24σ. $\sim$69 net counts from this source have been collected by ACIS-S in this observation and this allows us to perform a detailed analysis.

We found its X-ray spectrum can be well described by an absorbed power-law model with a photon index of $\Gamma_X = 2.7^{+1.4}_{-1.1}$ (Fig. 10). It yields a goodness of fit of $\chi^2 = 13.97$ for 21 dof. The best-fitting column absorption is found to be $n_H = 1.5^{+0.8}_{-0.5} \times 10^{23}$ cm^{-2} that is much larger than the total Galactic H I column density along the direction toward this source. Adopting this best-fitting model, the absorption-corrected X-ray flux becomes $F_X = 2.4 \times 10^{-12}$ erg cm^{-2} s^{-1} in 0.3–10 keV. On the other hand, its spectrum can also be fitted by an absorbed blackbody model and results in a comparable goodness of fit ($\chi^2 = 13.71$ for 21 dof). It yields an $n_H = 9.2^{+5.1}_{-3.4} \times 10^{22}$ cm^{-2} and a temperature of $kT = 1.3^{+0.4}_{-0.3}$ keV. The best-fitting normalization implies a thermal emission region with a radius of $\sim$10.6d_{kpc} m, where d_{kpc} is the distance to the source in unit of kpc. The best-fitting blackbody model implies an absorption-corrected X-ray flux to be $F_X \sim 3.0 \times 10^{-13}$ erg cm^{-2} s^{-1} in 0.3–10 keV.
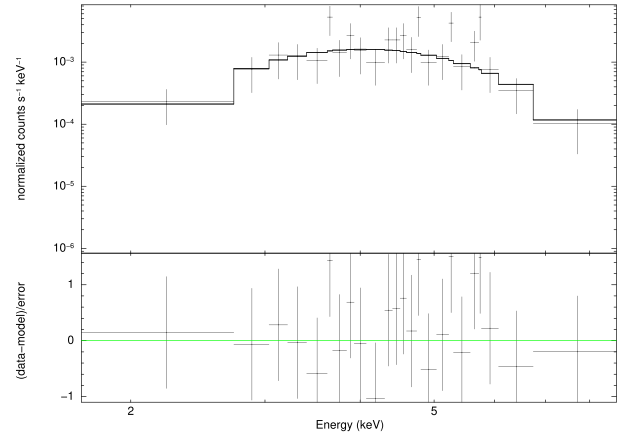

Figure 10. The X-ray spectrum of J14051_X1 as observed by *Chandra* ACIS-S with the best-fitting absorbed power law (upper panel) and contribution to the fitting residuals (lower panel).
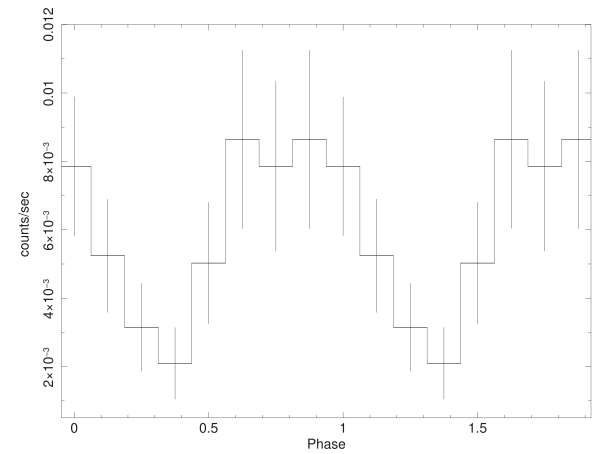

Figure 11. X-ray light curve of J14051_X1 in 0.5–7 keV as obtained by *Chandra* ACIS-S. It is folded at the period of $P = 1.4$ h.

We have also examined its X-ray temporal properties. Although the variability analysis with the Gregory–Loredo algorithm does not indicate any significant variability, a visual inspection of its barycentric-corrected light curve suggests a possible underlying structure. In particular, there appears to have two peaks separated by $\sim$5000 s that suggests a possible periodicity. Searches for the periodic signal around this value by epoch folding yield a candidate signal at $P \sim 5090$ s with $\chi^2 = 12.2$ for 7 dof. The X-ray light curve of J14051_X1 folded at this putative period is shown in Fig. 11. Although the statistical significance of this folded light curve for being different from a uniform distribution is low (pre-trial *p*-value $\sim$10 per cent), its apparently sinusoidal nature makes it as a promising candidate for further investigation.

Visual examination of the X-ray image of J14051_X1 suggests it is possibly extended. A close-up view of J14051_X1 is shown in Fig. 12. The source appears to be slightly elongated along the north-west–south-east orientation. Also, it apparently extends towards south-west. In order to further investigate its spatial nature, we compute its brightness profiles along the aforementioned orientations with sampling regions illustrated by the upper panels in Fig. 13. In the lower right-hand panel of Fig. 13, we show the brightness profile of J14051_X1 along the north-west–south-east orientation.
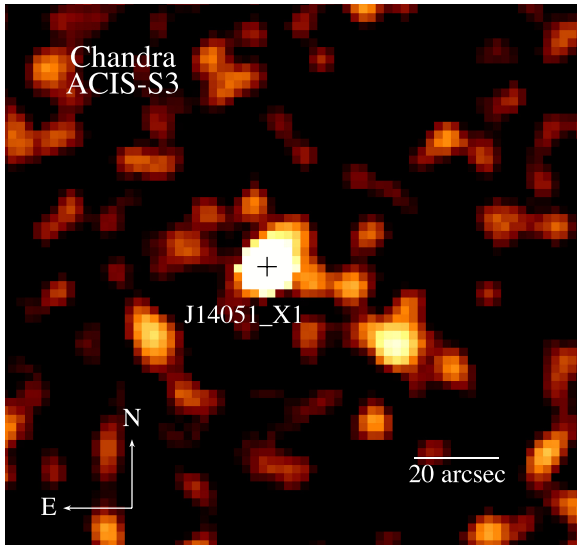
Figure 12. A smoothed image of the field around J14051_X1 as observed by *Chandra* ACIS-S3 in 0.3–8 keV. The black cross illustrates the X-ray position of J14051_X1 as given in Table 4. The source is apparently elongated along the north-west–south-east (NW–SE) orientation and it also appears to be extended towards south-west (SW).

The source appears to have an extent of ∼10 arcsec towards north-west. As J14051_X1 has an off-axis angle of ∼4.1 arcmin in this observation, the apparent elongation can be a result of distorted point spread function (PSF). To examine this, we have used the *Chandra Ray Tracer* (CHART) to simulate the PSF. The adopted inputs for simulating the PSF are the energy spectrum of J14051_X1 with the same exposure, roll, and off-axis angle as in the ACIS-S3 observation. Then we computed the brightness profile of the simulated data with the same set of sampling regions in the upper right-hand panel of Fig. 13. The result is displayed as the dotted line in the lower right-hand panel of Fig. 13, which matches the observed profile pretty well. Hence, we conclude that the elongation of J14051_X1 along the north-west–south-east orientation is due to the degraded angular resolution as a result of large off-axis angle.

On the other hand, the brightness profile for the south-western extended feature is shown in the lower left-hand panel of Fig. 13. The feature appears to have an extension of ∼20 arcsec towards south-west before it falls to the background. We have also compared the observed profile with the simulated PSF. In this direction, the profile of the simulated PSF falls to the background within the bin corresponds to the peak in the observed profile. Therefore, this ∼20 arcsec extent cannot be accounted by the distorted PSF. The S/N of this feature is ∼4σ. We have examined the Digitized Sky Survey optical image for the region of this feature. We do not find any optical counterpart to account for this putative extended X-ray feature.

We have also identified the IR counterpart of J14051_X1. Using the extinction of $A_v = 8.5$ as inferred from the Galactic H I column density, we constructed the extinction-corrected SED. Fitting a blackbody to this SED yields a temperature of $T_{bb} \sim 2013$ K and a emitting area with a radius of $R_{bb} \sim 6.6 d_{kpc}$ R⊙ with both T_{bb} and R_{bb} as free parameters.

3.2.8 3FHL J1626.3–4915

Part of the positional error ellipse of 3FHL J1626.3–4915 has been covered by a *Chandra* ACIS-I observation (Obs. ID: 13287)

on 2012 June 16 for an effective exposure of ∼10 ks. It is also partially covered by an *XMM–Newton* observation (Obs ID: 0403280201) on 2007 February 14. However, this observation was seriously contaminated by high background. After removing these contaminated time intervals, an effective exposure of ∼6 ks is remained in the *XMM–Newton* data. In the *Chandra* observation, two sources, J16263_X1 and J16263_X2, are detected. The brighter one J16263_X1 can also be detected in the short *XMM–Newton* exposure. The difference of its flux in these two frames is only ∼2σ. For J16263_X2, it is below the detection threshold in the *XMM–Newton* observation. This places a limit of >3.7σ on its long-term variability. Another source J16263_X3, which is not covered by the FoV of the *Chandra* observation, is detected by *XMM–Newton*. From the sources serendipitously detected in these observations, the probability of chance coincidence is found to be $P (n \geq 1) \sim 99$ and ∼61 per cent in the *Chandra* and *XMM–Newton* observation, respectively. For computing the F_X of all three detected sources as given in Table 4, we adopt a column absorption of $n_H = 1.9 \times 10^{22}$ cm^{-2} based on the H I estimate and their net count rates.

∼87 net counts are collected from J16263_X1 altogether from *Chandra* and *XMM–Newton* data. This allows us to carry out a more detailed analysis. We found that its X-ray spectrum can be fitted equally well with both absorbed power-law ($\chi^2 = 16.31$ for 23 dof) and absorbed blackbody models ($\chi^2 = 15.78$ for 23 dof). The best-fitting power-law model yields a column absorption of $n_H = 6.5^{+10.3}_{-6.5} \times 10^{21}$ cm^{-2}, a photon index of $\Gamma_X = 2.0^{+0.7}_{-0.6}$, and an unabsorbed flux $F_X = 2.7^{+3.8}_{-0.9} \times 10^{-13}$ in 0.3–10 keV. For the best-fitting blackbody model, it yields $n_H < 3.4 \times 10^{21}$ cm^{-2}, a temperature $kT = 0.9 \pm 0.1$ keV, emitting area with a radius of $R = 4.5^{+2.1}_{-4.5} d_{kpc}$ km, and an unabsorbed flux $F_X = (1.2 \pm 0.2) \times 10^{-13}$ in 0.3–10 keV. The goodness of fit for both models are comparable (see Table 6).

For J16263_X3, there are ∼130 net counts collected by *XMM–Newton*. By fitting its spectrum with an absorbed power law, we obtain the best-fitting results of $n_H = 8.4^{+2.4}_{-2.0} \times 10^{21}$ cm^{-2}, $\Gamma_X = 4.0^{+0.7}_{-0.6}$, and an unabsorbed flux $F_X \simeq 1.9 \times 10^{-12}$ in 0.3–10 keV. On the other hand, the best-fitting blackbody model yields $n_H = 1.6^{+1.9}_{-1.5} \times 10^{21}$ cm^{-2}, $kT = 0.4 \pm 0.1$ keV, an emitting area with a radius of $R = 68^{+40}_{-21} d_{kpc}$ m, and an unabsorbed flux $F_X \sim 1.2 \times 10^{-13}$ in 0.3–10 keV. Although the power-law model yields a better goodness of fit ($\chi^2 = 10.51$ for 23 dof), its photon index is too steep to account for any reasonable non-thermal emission scenario.

We have identified the optical/IR counterparts of J16263_X1 and J16263_X2. For J16263_X1, after correcting the extinction with $A_v = 8.9$ by assuming the total Galactic H I column density, its optical/IR counterpart can be described by a blackbody of $T_{bb} \sim 2000$ K and $R_{bb} \sim 1.1 d_{kpc}$ R⊙. However, its SED only has two data points and do not allow us to properly constrain its blackbody parameters and compute the uncertainties. For J16263_X2, we found that the adopted $A_v = 8.9$ might overcorrect the extinction and results in an unphysical high blackbody temperature. On the other hand, a possible counterpart of J16263_X2 is identified by *Gaia* and place an estimate on its distance to be 3.6 kpc.

3.2.9 3FHL J1747.2–2822

3FHL J1747.2–2822 is located along the line of sight towards the Galactic Centre. The 95 per cent γ-ray positional error ellipse of 3FHL J1747.2–2822 has been covered by two *Chandra* observations, Obs. IDs: 944 (2000 March 29; 100 ks) and 11795 (2010
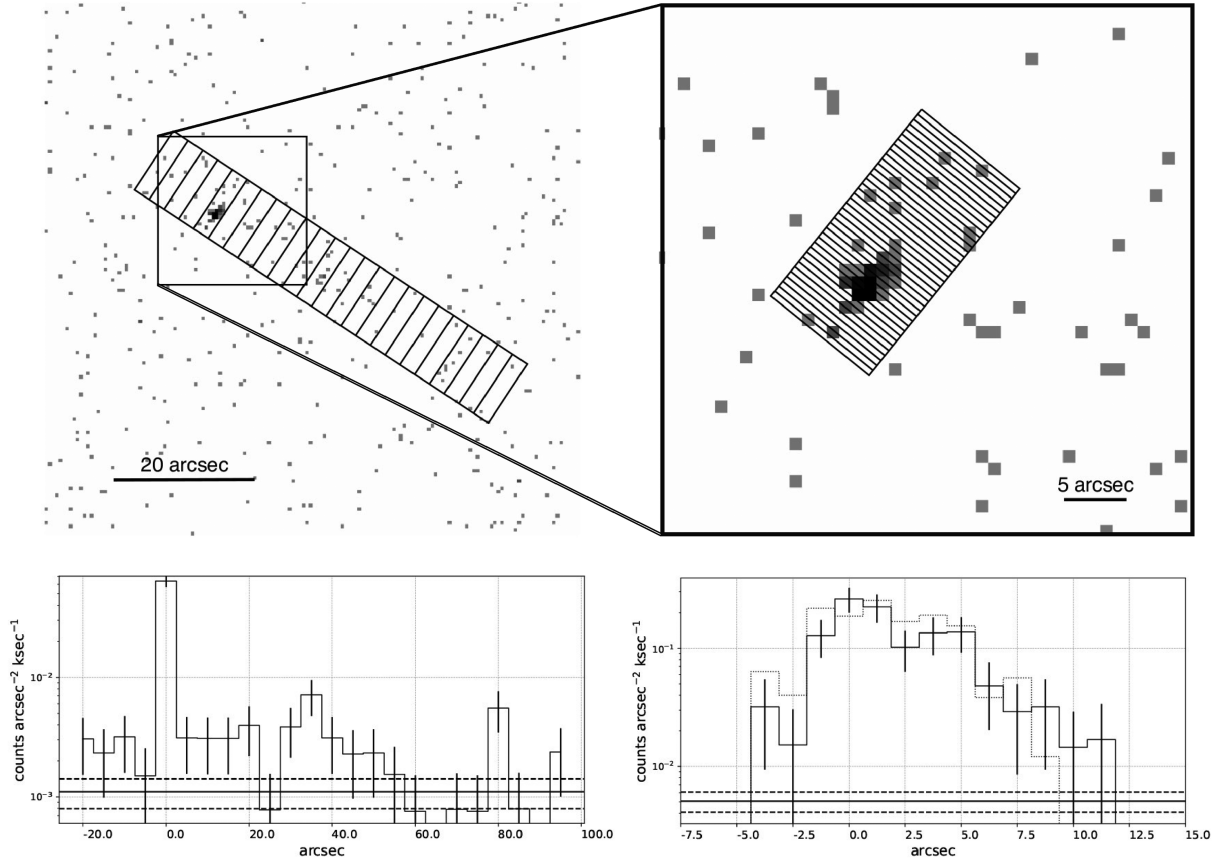
Figure 13. The brightness profile of the putative south-west (SW) extended feature associated with J14051_X1 (lower left-hand panel) as sampled from regions in the *Chandra* ACIS-S3 raw image (upper left-hand panel). The brightness profile of J14051_X1 along the north-west–south-east (NW–SE) orientation as sampled from the regions illustrated in the upper right-hand panel is displayed in the lower right-hand panel. The dotted line in this plot represents the expected profile from a point-like source. The average background level and its 1σ deviation are indicated by horizontal lines that were calculated by sampling from the source-free regions.

July 29; 98 ks), and five *XMM–Newton* observations, Obs. IDs: 0802410101 (2018 April 2; 99 ks), 0694641401 (2012 September 30; 34 ks), 0694641301 (2012 September 26; 47 ks), 0694640601 (2012 September 6; 41 ks), and 0203930101 (2004 September 4; 33 ks).

Using the *Chandra* observation in 2010, eight X-ray sources were detected within the γ-ray ellipse. In the 2000 *Chandra* observation, only J17472_X1, J17472_X2, J17472_X4, J17472_X5, and J17472_X6 can be detected. In comparing these two frames, J17472_X5 is found to be variable at the level of 4.3σ. On the other hand, the non-detections of J17472_X3, J17472_X7, and J17472_X8 place limits on their variabilities to be $>1.9\sigma$, $>1.1\sigma$, and $>0.3\sigma$, respectively. In all the *XMM–Newton* observations, only J17472_X1 can be detected. Its flux as measured by these observations are all consistent with that obtained in *Chandra* observation.

Their unabsorbed F_X given in Table 4 are estimated by their count rate detected in the 2010 *Chandra* observation with the total Galactic H I column density $n_H = 1.2 \times 10^{22}$ cm^{-2} in that direction. Since 3FHL J1747.2–2822 lies along the direction towards the Galactic Centre, the spatial density of the X-ray sources is rather high. Using the serendipitous X-ray sources detected in these data, $P(n \geq 1)$ is estimated to be as high as ~ 100 per cent in all observations.

Among the detected X-ray sources, J17472_X1 is the brightest and is detected by all observations. However, we found that it

coincides with the giant molecular cloud Sgr B2. The association is further confirmed by the detection of the iron line at 6.4 keV that is likely to be originated from the interaction between the hard X-rays from the Sgr A* and the cloud (Dogiel et al. 2015). Therefore, J17472_X1 is not the main interest for this work and will not be further concerned. For the other seven X-ray sources, their net counts are all less than 50 and no further analysis will be performed.

We have also identified an optical/IR counterpart of J17472_X8. Using an extinction of $A_v = 5.7$ as inferred from the total Galactic H I column density, a blackbody fitting to the extinction-corrected SED yields a temperature of $T_{bb} = 1900 \pm 200$ K and an emitting area with a radius of $R_{bb} = 11 \pm 2\, d_{kpc}$ R$_\odot$.

3.2.10 3FHL J0737.5+6534

3FHL J0737.5+6534 is located very far away from the Galactic plane with $b \sim 29°$. Its γ-ray positional error ellipse has been covered by three *Chandra* observations, Obs. IDs: 4630 (2004 December 22; 50 ks), 4629 (2004 October 3; 45 ks), and 4628 (2004 August 23; 47 ks), and four *XMM–Newton* observations, Obs. IDs: 0729560901 (2014 April 4; 2.7 ks), 030186301 (2005 October 11; 9.7 ks), 0164560901 (2004 September 12; 56 ks), and 0150651101 (2003 April 30; 4.3 ks).

Table 7. X-ray spectral properties of J07375_X1 at different epochs.

Obs. date (yyyy-mm-dd)	χ^2	dof	Γ_X	$F^{unabs}_{0.3-10\,keV}$ $(10^{-13}$ erg cm^{-2} s$^{-1})$
2003-04-30	16.71	17	$2.07^{+1.21}_{-0.63}$	$0.32^{+0.11}_{-0.07}$
2004-08-23	8.64	15	1.67 ± 0.11	$0.65^{+0.06}_{-0.05}$
2004-09-12	11.37	20	2.01 ± 0.08	0.43 ± 0.02
2004-10-03	6.33	15	1.84 ± 0.10	$0.79^{+0.06}_{-0.05}$
2004-12-22	17.25	16	1.88 ± 0.11	0.58 ± 0.04
2005-10-11	5.74	18	$2.56^{+0.43}_{-0.40}$	0.21 ± 0.04
2014-04-04	8.48	14	$1.61^{+0.53}_{-0.51}$	$0.39^{+0.18}_{-0.13}$

Table 8. X-ray spectral properties of J07375_X2 at different epochs.

Obs. date (yyyy-mm-dd)	χ^2	dof	Γ_X	$F^{unabs}_{0.3-10\,keV}$ $(10^{-13}$ erg cm^{-2} s$^{-1})$
2004-08-23	10.08	15	1.00 ± 0.21	0.20 ± 0.04
2004-10-03	13.30	13	$1.39^{+0.26}_{-0.23}$	$0.20^{+0.04}_{-0.03}$
2004-12-22	13.29	14	0.98 ± 0.18	$0.36^{+0.06}_{-0.05}$
2003-04-30	9.97	18	$1.73^{+0.73}_{-0.66}$	$0.21^{+0.12}_{-0.09}$
2004-09-12	29.06	20	$1.19^{+0.19}_{-0.18}$	$0.18^{+0.03}_{-0.02}$
2005-10-11	11.10	13	$0.04^{+0.87}_{-0.83}$	$0.25^{+0.20}_{-0.16}$
2014-04-04	1.43	4	$1.37^{+2.17}_{-1.37}$	$0.27^{+21.34}_{-0.20}$

Eight X-ray sources have been found within its γ-ray error ellipse by using the longest *Chandra* observation at 2004 December. Based on their count rate obtained from this observation and the adopted column absorption of $n_H = 4.5 \times 10^{20}$ cm^{-2} that is consistent with the total Galactic H I column density in that direction, we estimated their unabsorbed F_X in Table 4. J07375_X1 is the brightest X-ray sources among them. Its flux is found to be significantly variable at a level as high as $\sim 12\sigma$. The shortest time-scale of its X-ray variability found in this study is ~ 4 months. J07375_X2 and J07375_X5 also exhibit long-term X-ray variability at the level up to 8σ and 4σ among these observations.

J07375_X1 and J07375_X2 have 1096 and 454 net counts collected from all these archival data, respectively, and therefore we have carried out a more detailed analysis. Their photon statistics from each observation are high enough to allow us performing multi-epoch spectral analysis. By fixing n_H at 4.5×10^{20} cm^{-2}, the best-fitting parameters in each epoch of J07375_X1 and J07375_X2 are summarized in Tables 7 and 8, respectively. Evidences for spectral variabilities are found from both sources.

Among eight X-ray sources, six of them have optical/IR counterparts identified. The results of blackbody fitting to their SEDs are summarized in Table 5. Their inferred low temperatures and small radii suggest they can possibly be late-type stars. For J07375_X3, counterpart has also been found by *Gaia* that suggests a distance of 1.6 kpc.

4 SUMMARY AND DISCUSSIONS

With an optimal set of features selected by RFE algorithm (see Table 1 and Fig. 1), a supervised classification model is built from a training set of labelled PSR/NON_PSR 3FHL objects. Using this model, we have selected 27 PSR-like objects with a nominal accuracy of ~ 98 per cent from the unknown 3FHL sources for identification campaign (see Table 3). Utilizing the archival X-ray

data, we have found X-ray counterparts from 10 3FHL PSR-like candidates (see Table 4 and Fig. 4). These identifications allow us to systematically constrain the positions of the potential X-ray counterparts to arcsecond accuracies, estimate the X-ray to γ-ray flux ratios F_X/F_γ and temporal variabilities. Except for J18007_X8 and J17472_X8, the F_X/F_γ for all the other X-ray sources conform with that for the known pulsars detected in the energy range of 10 GeV to 2 TeV. For the sources with their X-rays found to be significantly varying in a given observation window and/or across different epochs, their flux variabilities make them less likely to be a typical pulsar that has rather stable X-ray emission. On the other hand, we cannot exclude the possibility of these variable X-ray sources as γ-ray binaries. Also, their X-ray positions enable us to search for the optical/IR counterparts and estimate the surface temperatures and sizes of the possible companion stars by assuming a blackbody model (see Table 6).

For those have more than 50 net counts collected from the archival X-ray data, we have carried out more detailed analysis. Among them, J18233_X1 that is associated with 3FHL J1823.3–1339 is one of the most interesting source. It is very likely to be the X-ray and γ-ray counterpart of the globular cluster Mercer 5 (cf. Fig. 6). The association between J18233_X1 and Mercer 5 is supported by the consistency between the column absorption obtained from the X-ray spectral fitting and that deduced from the optical extinction. On the other hand, the association between 3FHL J1823.3–1339 and Mercer 5 is suggested by the agreement between its γ-ray luminosity L_γ at the distance of the globular cluster and the general trend of L_γ–[Fe/H] as observed in the γ-ray globular cluster population (Hui et al. 2011).

Because of the frequent stellar encounters, globular clusters are efficient in producing compact binaries, including MSPs, through dynamical interactions (Pooley et al. 2003; Hui, Cheng & Taam 2010). It is a general consensus that the γ-ray emission from a globular cluster is originated from its MSPs. Therefore, we speculate that Mercer 5 is hosting a MSP population awaited to be discovered. Pulsar searches targeted at this cluster are encouraged to examine this assertion.

There are two different scenarios in explaining the γ-ray emission mechanism of a globular cluster. While their γ-rays can be collectively contributed by the magnetospheric radiation from the MSPs (Abdo et al. 2010), it is possible that the inverse Compton scattering (ICS) between the relativistic pulsar wind and the ambient soft photons can result in the observed γ-rays (Cheng et al. 2010). The ICS scenario is suggested by the correlation between L_γ and the energy densities of the ambient soft photon fields (Hui et al. 2011). Such scattering can boost the soft photons to an energy >10 GeV (Cheng et al. 2010). As the γ-ray spectrum of a pulsar typically has an exponential cut-off at a few GeV, their magnetospheric radiation is unlikely to have significant contribution in the hard γ-ray band. Therefore, the globular clusters detected at energies >10 GeV can help us to constrain the parameters of the ICS model (Cheng et al. 2010). Although there are 30 γ-ray globular clusters have been identified in the *Fermi* LAT 8-year Point Source Catalog (Abdollahi et al. 2020), only two of them, 47 Tuc and Terzan 5, are included in the 3FHL catalogue. On the other hand, fig. A3 in de Menezes, Cafardo & Nemmen (2019) shows that 2MS-GC01, NGC 6440, and NGC 2808 seem to have emission above 10 GeV. The survey with the upcoming CTA holds the potential in further expanding the population of hard γ-ray globular clusters.

Apart from MSPs, globular clusters also host different classes of compact X-ray binaries (e.g. low-mass X-ray binaries, cataclysmic variables). Ascribing to the relatively poor spatial resolution of

XMM–Newton, the X-ray counterpart of Mercer 5, J18233_X1, identified in this work is likely resulted from a blend of unresolved X-ray point source population. Its X-ray spectrum can be well described by a power-law model with $\Gamma_X \sim 1.1$ (Fig. 7) that is apparently harder than the faint unresolved X-ray populations found in the other clusters (Hui, Cheng & Taam 2009). A spectral imaging analysis with high spatial resolution by *Chandra* is necessary to resolve and classify the X-ray binaries in Mercer 5.

Another interesting identification in our campaign is 3FHL J1405.1–6118 and its promising X-ray counterpart J14051_X1. The X-ray spectrum of J14051_X1 can be described by a power law of $\Gamma_X \sim 2.7$ with a large column absorption $n_H \sim 1.5 \times 10^{23}$ cm^{-2} (Fig. 10). Such large X-ray absorptions are commonly seen in the high-mass X-ray binaries (HMXBs; Paul et al. 2017). Very recently, a γ-ray periodic modulation of $P_b \sim 13.7$ d in 0.2–500 GeV has been discovered that makes 3FHL J1405.1–6118 (= 4FGL J1405.1–6119) the third γ-ray binary found from the initial discovery of periodic modulation of the LAT light curve (Corbet et al. 2019). X-ray modulation of J14051_X1 at the same period has also been found by *Swift* XRT (cf. fig. 4 in Corbet et al. 2019). Taking the phase zero at MJD 56498.7, *Chandra* exposure used in our work corresponds the orbital phase of $\sim$0.07–0.08 that is not included in Corbet et al. (2019). Using our best-fitting spectral model and with the aid of PIMMS, the flux observed by *Chandra* translates into a *Swift* XRT count rate of $\sim 10^{-3}$ counts s^{-1} that is consistent with that in the phase interval of $\sim$0.03–0.25 as reported in the table 1 of Corbet et al. (2019).

For the optical/IR counterpart of 3FHL J1405.1–6118, the blackbody fitting to its SED yields a temperature of $T \sim 2000$ K and a radius of $R \sim 7$ R$_\odot$ in the case that we adopt $A_v = 8.5$, $d = 1$ kpc, and with both T_{bb} and R_{bb} as free parameters. On the other hand, based on the near-IR spectroscopy, Corbet et al. (2019) identify the counterpart as an O6 III star. To examine whether this inference can be consistent with our photometric result, we redo the blackbody fitting with T_{bb} fixed at 40 000 K that is typical for O stars and adopt the mean-derived extinction of $A_v = 31.6$ ($E(B-V) = 10.2$) reported by Corbet et al. (2019). At a distance of $d = 7.7$ kpc (Corbet et al. 2019), it yields a radius of $R_{bb} = 12.9 \pm 0.8$ R$_\odot$ that is consistent with the expected size for an O6 III star.

While Corbet et al. (2019) have found the orbital period of $\sim$13.7 d, the X-ray light curve observed by *Chandra* suggests a periodicity candidate at $P \sim 1.4$ h (Fig. 11). For the HMXBs with the X-ray pulses from the neutron stars detected, their spin periods span a range from $\sim$0.03 s to $\sim$4 h (Liu, van Paradijs & van den Heuvel 2006). Therefore, this signal can possibly be originated from the neutron star rotation. Deeper follow-up observations are strongly encouraged to examine this putative signal.

Apart from the periodic signal candidate, this short *Chandra* observation also reveals a putative extended X-ray feature associated with J14051_X1 at a significance of $\sim 4\sigma$ (Figs 12 and 13). A deeper observation is required to confirm its spatial nature with higher S/N and examine if there is any spectral variation across it. Evidences of such X-ray features have been found from a number of γ-ray binaries, including PSR B1259−63/LS 2883 (Pavlov et al. 2015), LS I +61 303 (Paredes et al. 2007), and LS 5039 (Durant et al. 2011). Except for PSR B1259−63/LS 2883, the nature of the compact objects for the other γ-ray binaries remains unknown. For PSR B1259−63/LS 2883, its extended X-ray feature can be resulted from synchrotron radiation emitted by the relativistic particles accelerated at the shock between the pulsar wind and the massive star outflow (Tavani & Arons 1997). On the other hand, if the γ-ray binary is powered by a microquasar,

the extended X-ray nebula can be originated from the relativistic particles produced by the Blandford–Znajek process (Blandford & Znajek 1977) or from a magnetohydrodynamic (MHD) jet. Pulsar searches of 3FHL J1405.1–6118 can help to discriminate these two competing scenarios.

REFERENCES

Abdo A. A. et al., 2009, Science, 325, 845
Abdo A. A. et al., 2010, A&A, 524, A75
Abdo A. A. et al., 2013, ApJS, 208, 17
Abdollahi S. et al., 2020, ApJS, 247, 33
Acero F. et al., 2015, ApJS, 218, 23
Aharonian F. et al., 2008, A&A, 481, 401
Ajello M. et al., 2017, ApJS, 232, 18
Bailer-Jones C. A. L., Rybizki J., Fouesneau M., Mantelet G., Andrae R., 2018, AJ, 156, 58
Baumgardt H. et al., 2019, MNRAS, 482, 5138
Blandford R. D., Znajek R. L., 1977, MNRAS, 179, 433
Chambers K. C. et al., 2016, preprint (arXiv:1612.05560)
Cheng K. S., Chernyshov D. O., Dogiel V. A., Hui C. Y., Kong A. K. H., 2010, ApJ, 723, 1219
Clark C., 2017, in Proceedings of Science Vol. 312, 7th International Fermi Symposium (IFS2017), SRL, Trieste, Italy
Corbet R. H. D. et al., 2019, ApJ, 884 , 93
Cui Y., Yeung P. K. H., Tam P. H. T., Pühlhofer G., 2018, ApJ, 860, 69
Cutri R. M. et al., 2012, VizieR On-line Data Catalog: II/311
de Menezes R., Cafardo F., Nemmen R., 2019, MNRAS, 486, 851
Dogiel V. A. et al., 2015, ApJ, 809, 48
Durant M. et al., 2011, ApJ, 735, 58
Fitzpatrick E. L., 1999, PASP, 111, 63
Gaia Collaboration et al., 2018, A&A, 616, A1
Gregory P. C., Loredo T. J., 1992, ApJ, 398, 146
Güver T., Özel F., 2009, MNRAS, 400, 2050
Hampton E. J., Rowell G., Hofmann W., Horns D., Uchiyama Y., Wagner S., 2016, J. High Energy Astrophys., 11, 1
Hui C. Y., 2018, J. Korean Astron. Soc., 51, 171
Hui C. Y., Cheng K. S., Taam R. E., 2009, ApJ, 700, 1233
Hui C. Y., Cheng K. S., Taam R. E., 2010, ApJ, 714, 1149

Hui C. Y. et al., 2011, ApJ, 726, 100
Hui C. Y. et al., 2015, ApJ, 809, 68
Hui C. Y., Lee J., Takata J., Ng C. W., Cheng K. S., 2017, ApJ, 834, 120
Kalberla P. M. W. et al., 2005, A&A, 440, 775
Kaur A., Ajello M., Marchesi S., Omodei N., 2019, ApJ, 871, 94
Khan R., Stanek K. Z., Kochanek C. S., Sonneborn G., 2015, ApJS, 219, 42
Kong A. K. H., Hui C. Y., Cheng K. S., 2010, ApJ, 712, L36
Kong A. K. H. et al., 2012, ApJ, 747, L3
Leung A. P., Tong Y., Li R., Luo S., Hui C. Y., 2017, in Proceedings of Science Vol. 312, 7th International Fermi Symposium (IFS2017), SRL, Trieste, Italy
Liu Q. Z., van Paradijs J., van den Heuvel E. P. J., 2006, A&A, 455, 1165
Longmore A. J. et al., 2011, MNRAS, 416, 465
Luo S., Leung A. P., Hui C. Y., Li K. L., 2020, MNRAS, 492, 5377
Manchester R. N. et al., 2005, AJ, 129, 1993
Mercer E. P. et al., 2005, ApJ, 635, 560
Minniti D., Lucas P., VVV Team, 2017, VizieR On-line Data Catalog: II/348
Nolan P. L. et al., 2012, ApJS, 199, 31

Paredes J. M. et al., 2007, ApJ, 664, L39
Paul B., 2017, J. Astrophys. Astron., 38, 39
Pavlov G. G. et al., 2015, ApJ, 806, 192
Peñaloza F. et al., 2015, PASP, 127, 329
Pooley D. et al., 2003, ApJ, 591, L131
Saito R. K. et al., 2012, A&A, 537, A107
Saz Parkinson P. M., Xu H., Yu P. L. H., Salvetti D., Marelli M., Falcone A. D., 2016, ApJ, 820, 8
Spitzer Science Center, 2009, VizieR On-line Data Catalog: II/293
Takata J. et al., 2017, ApJ, 836, 241
Tam P. H. T. et al., 2011, ApJ, 729, 90
Tam P. H. T., He X.-B., Pal P. S., Cui Y., 2018, ApJ, 862, 165
Tavani M., Arons J., 1997, ApJ, 477, 439

This paper has been typeset from a TEX/LATEX file prepared by the author.